



# Observational data provide valuable insights for glacier thickness reconstruction in High Mountain Asia

Gillian M. A. Smith<sup>1</sup>, Daniel N. Goldberg<sup>2</sup>, Guillaume Jouvét<sup>3</sup>, James R. Maddison<sup>1</sup>, and Hamish D. Pritchard<sup>4</sup>

<sup>1</sup>School of Mathematics and Maxwell Institute for Mathematical Sciences, The University of Edinburgh, Edinburgh, United Kingdom

<sup>2</sup>School of GeoSciences, The University of Edinburgh, Edinburgh, United Kingdom

<sup>3</sup>Institute of Earth Surface Dynamics, University of Lausanne, Lausanne, Switzerland

<sup>4</sup>British Antarctic Survey, Cambridge, United Kingdom

**Correspondence:** Gillian M. A. Smith (g.smith@ed.ac.uk)

**Abstract.** Mountain glaciers provide an irreplaceable water resource in High Mountain Asia, with a significant proportion of water input to rivers coming from glacial meltwater. However, the volume of water held in these glaciers and their evolution over the coming decades is subject to great uncertainty. The reliability of existing glacier ice thickness estimates in High Mountain Asia is limited by the use of low-order models, known to be locally unreliable on mountain glaciers, to describe the relationship between ice velocity and thickness, and by the scarcity of measured thicknesses available for constraint and validation at the time those estimates were produced. We use the Instructed Glacier Model (v2.2.3), a deep-learning-based high-order ice flow model with the capability to invert observed glacier surface velocity for ice thickness, to construct an estimated thickness map of Bhote Kosi glacier. Our thickness inversion is constrained using data collected via a novel airborne radar method for measuring ice thickness. We perform an in-depth case study, carefully justifying inversion parameter choices and quantifying the accuracy of our results. We demonstrate that in the absence of thickness observations, results can be optimized via the use of an L-curve to select the regularization parameter, with significant bias in the unconstrained results, but comparable accuracy to leading thickness estimates. We find that while thickness-constrained inversions are able to correct the modelled thickness field where there is limited information from observed surface velocity, cross-validation experiments demonstrate that the “interpolative power” of thickness observations is weak.

## 15 1 Introduction

Forecasting the future evolution of glaciers is vital to predict the volume of ice left in the future, the potential rise in sea level caused by glacier mass loss, and the likelihood of natural hazards such as glacial lake outburst floods (Nie et al., 2021). Even though the world’s glaciers contain considerably less mass than the Greenland and Antarctic ice sheets (Farinotti et al., 2019; Morlighem et al., 2017; Pritchard et al., 2025), in recent years they have been responding faster to climate change, with a greater total mass loss than each of the ice sheets individually (Hugonnet et al., 2021). The total mass of glaciers worldwide is



predicted to decrease by approximately one quarter to one half in the period 2015–2100, depending on global mean temperature increase (Rounce et al., 2023).

The High Mountain Asia (hereafter abbreviated to HMA) region covers a large area, from the Tian Shan and Hindu Kush mountains in the west to the Himalaya in the east. Leading estimates are clear that the region contains more ice than any other region on Earth outside the polar regions, but there is still significant uncertainty about the quantity of water held in HMA's glaciers (Farinotti et al., 2019; Millan et al., 2022). It has been estimated that glaciers in HMA have been responsible for around 8–10% of total worldwide glacier mass loss in the early twenty-first century (Wouters et al., 2019; Hugonnet et al., 2021; Jakob and Gourmelen, 2023). Rounce et al. (2020) predicts that HMA glaciers are expected to continue to lose a substantial proportion of their mass by 2100, although future glacier mass loss in HMA is hard to quantify with certainty, due to uncertainty in both the future climate and the models used. Of particular concern is the impact on HMA's water resources, as glaciers in the region act as a water reserve that protects rivers and downstream populations from drought. Many rivers in the region receive a large proportion of their input from glacial meltwater, and may lose this input over the coming decades, transitioning (perhaps abruptly) from a glacier-melt-buffered “glacio-pluvial” regime to a mostly pluvial regime dependent on recent precipitation. An estimated 800 million people in the region are dependent in part on the water supply from these rivers (Pritchard, 2019).

With an estimate of the total volume or equivalent mass of water held within a set of glaciers, various glaciological and hydrological questions can be addressed. Potential future sea level rise attributed to a region's glaciers can be quantified from their estimated total mass (Farinotti et al., 2019; Millan et al., 2022). Particularly relevant for HMA is that information about glacier mass and mass loss can aid in making predictions about flooding and future water supply (Pritchard, 2019; Nie et al., 2021).

Additionally, knowledge of thickness distribution (as opposed to total volume) of a glacier is a necessary initial condition for glacier evolution modelling, whereby the future shape and size of a glacier is estimated. Unlike other variables which can be derived from satellite data (such as glacier extent, surface velocity, and change in surface elevation), there is no spaceborne option for measuring ice thickness. Direct measurement of ice thickness can only be obtained through survey in close proximity, with either ground-based or airborne methods. Among the many factors limiting the scope of glacier ice thickness measurement field campaigns are time, monetary cost, equipment available, terrain, altitude, weather, and political constraints. Due to these limitations, glacier ice thickness observations in all regions are generally sparse in both space and time. Accurate estimation of ice thickness distribution is therefore a common, yet unresolved problem in glaciology.

Historically, HMA glaciers have had particularly poor observational coverage, with only 88 out of more than 95 000 glaciers having a thickness measurement in the worldwide Glacier Thickness Database (GlaThiDa), compared with, for example, 175 out of less than 4000 glaciers in Central Europe (Welty et al., 2020). This is partially because glaciers in the region are often debris-covered and have rough surfaces with significant crevassing, making ground-based surveys difficult to carry out. Airborne surveys are able to survey these glaciers more efficiently, but the debris cover and narrow valleys in which these glaciers are found still cause challenges for measuring the ice with radar equipment.



55 Pritchard et al. (2026) present thickness observations for 13 glaciers (as outlined by RGI Consortium, 2017) in the Himalaya region near Everest, via the use of a bespoke airborne radar system deployed by helicopter and developed specially for use in the region. The increased manoeuvrability of helicopters at high altitude (versus that of fixed-wing aircraft, such as those typically used for thickness surveys of the polar ice sheets) is what made this study possible. Additionally, the use of a low-frequency radar allowed for better penetration into the ice in this region, which is typically covered with debris and has a high  
60 water content. This study approximately doubled the combined length of all surveyed thickness profiles in the entire HMA region, opening up new possibilities for calibration and validation of thickness estimates.

Ice thickness estimation (often termed thickness “inversion”) has become considerably more tractable in recent years due to the increase in quality and availability of satellite data. While the first worldwide glacier thickness estimation study was performed by Huss and Farinotti (2012), based on mass conservation principles and without using any information about the  
65 surface velocity, surface velocity data is now a prerequisite for many ice thickness estimation methods (Farinotti et al., 2017). There now exist worldwide glacier surface velocity products derived from feature tracking of high-resolution satellite imagery (Millan et al., 2022; Gardner et al., 2025). Change in surface elevation is another satellite-derived data product that is required for many of the thickness estimation methods that are based on mass conservation (Farinotti et al., 2017). Hugonnet et al. (2021) mapped change in surface elevation for all glaciers on Earth, using 20 years’ worth of satellite data from multiple  
70 sources. However, one challenge that persists in the estimation of ice thickness, is that in most locations there is no available “true” thickness to validate a model: for the vast majority of glaciers there are no thickness observations, and not all glaciers with observations have extensive coverage across the glacier (Welty et al., 2020).

The first phase of the Ice Thickness Models Intercomparison eXperiment (ITMIX, Farinotti et al., 2017) focused on glacier ice thickness estimation methods which do not use thickness observations at all to compute their thickness estimate, emulating  
75 the situation where there are no observational data available, which is the case for most glaciers. They found that thickness estimates vary depending on method, and that averaging the results of several methods is a viable strategy to obtain an accurate result. The second phase of ITMIX (ITMIX2, Farinotti et al., 2021), on the other hand, focused on validation of models which do calibrate to available thickness observations. ITMIX2 performed experiments where various subsets of the available thickness profiles were removed from the calibration, and the error of the resulting thickness field was then evaluated against  
80 the removed profiles. In the statistics and machine learning fields, this technique is known as cross-validation (Picard and Cook, 1984). The results of these experiments demonstrated that even limited sets of thickness observations are effective for reducing model bias (i.e. constraining volume), and that the spatial distribution of thickness observations has a weak effect on the quality of estimates.

Farinotti et al. (2019) averaged the results of several different methods to obtain a “consensus” estimate, based on the  
85 findings from Farinotti et al. (2017) that estimates vary widely between models, and the “law of large numbers” principle that ensemble means are expected to converge to the true value with increasing number of realizations. Millan et al. (2022) produced thickness estimates for glaciers worldwide by taking advantage of a high-resolution surface velocity dataset, directly inverting the shallow ice approximation (SIA) to obtain a simple relation between thickness and surface velocity. The results of Farinotti et al. (2019) and Millan et al. (2022) are currently widely used by the glacier modelling community, with several



90 studies building on these results (e.g. Immerzeel et al. (2020); Sommer et al. (2020); Khanal et al. (2021); Zheng et al. (2021);  
Bosson et al. (2023); Zekollari et al. (2024)). Hereafter we refer to the thickness estimates of Farinotti et al. (2019) and Millan  
et al. (2022) as the “consensus” estimate and “Millan” estimate respectively.

Other glacier and ice sheet inversion studies focus on attempting to estimate physical parameters related to basal sliding  
from observed velocities, often using adjoint methods, which are not limited to the SIA, but require lengthy manual deriva-  
95 tion (MacAyeal, 1992; Goldberg and Heimbach, 2013). Recent advances in the field of machine learning, including automatic  
differentiation and optimization libraries such as Tensorflow (Abadi et al., 2015) and Keras (Chollet, 2015), as well as the  
development of new optimizers based on stochastic gradient descent (e.g. Kingma and Ba, 2017), have opened up new pos-  
sibilities for solving inverse problems in glaciology. Steidl et al. (2025) constructed a physics-informed neural network, based  
on mass conservation, to estimate the thickness of glaciers in Svalbard. Maffezzoli et al. (2025) used gradient-boosted trees,  
100 another machine learning technique, to estimate the thickness of glaciers worldwide, with error comparable to the consensus  
and Millan estimates. Schmitt et al. (2025) presented a time-dependent inversion method which aims to create a dynamically  
consistent initialization of a glacier using the 4DVar data assimilation technique and automatic differentiation.

The Instructed Glacier Model (Jouvet and Cordonnier, 2023), hereafter abbreviated as IGM, is a novel deep-learning-based  
glacier model, which has shown promise for both prognostic (forecast) and diagnostic (state estimation) modelling. As an  
105 emulator for the Blatter-Pattyn (also known as first-order approximation) equations (Pattyn, 2003), it has been shown to eval-  
uate orders of magnitude faster than traditional Stokes-solving methods, excluding training time (Jouvet et al., 2022), and is  
equipped with a module that performs ice thickness inversion via a minimization approach (Jouvet, 2023). Cook et al. (2023)  
used IGM to first estimate current glacier thickness of the entire European Alps, and then to compute forecasts on a short (less  
than 50 years) time scale, on the basis that using the same physical model for both inversion and forward evolution will help to  
110 overcome the initial non-physical effects often experienced by glacier evolution models when modelling over such a short time  
scale. Frank and van Pelt (2024) and van Pelt and Frank (2025) used IGM for thickness inversion of glaciers in Scandinavia  
and Svalbard, although only as a forward model, with the authors opting for their own inversion method. The IGM inversion  
method has also been used for estimating surface mass balance of avalanching glaciers (Kneib et al., 2024).

In this study, we present in-depth analysis of the process of estimating the thickness of a previously unmeasured glacier in  
115 the Himalaya region. We use and scrutinize an inversion method based on cost minimization, making careful and methodical  
choices regarding the inversion parameters. We first investigate how well ice thickness can be reconstructed with knowledge of  
ice surface velocity alone, using the L-curve technique (Hansen and O’Leary, 1993) to find an optimal value for a key inver-  
sion meta-parameter. We use recently reported thickness observations from Pritchard et al. (2026) to validate our estimate, and  
compare our results with the Millan estimate. Then, we introduce the thickness data for calibration of the ice thickness, per-  
120 forming cross-validation experiments to assess the influence of spatial distribution of thickness observations. We demonstrate  
that parameter choices can strongly influence results, and consider the value added by an entirely new dataset of thickness  
observations.



## 2 Model, data, and methodology

Our thickness inversion is based on the method described in Jouvét (2023). This method relies on an ice-flow model emulator  
125 in the form of a convolutional neural network (CNN), as described in Jouvét and Cordonnier (2023), implemented in the  
framework of the Instructed Glacier Model (IGM). The emulator’s role is to replace the solving of the Blatter-Pattyn equations  
(Pattyn, 2003) for the three-dimensional velocity field, given the shape of the glacier and parameters representing the viscosity  
and basal sliding. IGM is also equipped with an inversion module, whose purpose is to estimate unknown variables based on  
available observational data, using the emulator as a forward model. In this section we summarise the inversion algorithm and  
130 outline our methodology for a detailed case study on one glacier in the Himalaya region.

### 2.1 Instructed Glacier Model

The IGM emulator is a convolutional neural network (CNN) that takes as input two-dimensional arrays of glacier thickness  $h$ ,  
surface topography  $s$ , Arrhenius factor  $A$  (a number that determines the ice viscosity; Glen, 1953), and a sliding coefficient  
 $c$  (based on a Weertman sliding law; Schoof and Hewitt, 2013), and outputs both horizontal velocity components  $u, v$  as  
135 three-dimensional arrays (Jouvét and Cordonnier, 2023, Figure 3). All variables are defined over a rectangular domain  $\Omega$ , and  
on a structured uniform orthogonal axis-aligned grid with cell width  $H$ . Each input array has dimensions  $N_x \times N_y$  (width  
times height of the domain  $\Omega$  in terms of number of cells), and each output array has dimensions  $N_x \times N_y \times N_z$ , where  $N_z$   
represents the number of vertical layers. The neural network can be represented as follows, where the subscript  $(\cdot)_H$  denotes  
the discretized variable:

$$140 \mathcal{N}_\lambda : (h_H, s_H, A_H, c_H) \mapsto (u_H, v_H). \quad (1)$$

Hereafter we will drop the subscript  $(\cdot)_H$  for clarity, with the understanding that all variables are discretized within IGM.

As described in Jouvét and Cordonnier (2023), the weights  $\lambda$  of the CNN are trained to minimise the energy functional  
associated with the Blatter-Pattyn model (Pattyn, 2003), thereby replacing the solver that would usually be present in a glacier  
model. This approach is inspired by physics-informed neural networks (PINNs), but differs in two important ways: the inputs  
145 to the neural network are fields defined on the entire horizontal grid, rather than spatial coordinates, and the cost (loss) function  
is the energy functional (similar to the “variational PINN” or “VPINN” described by Kharazmi et al., 2019), not the residual  
of the equations and boundary conditions.

We use a pretrained CNN (available from the IGM repository on GitHub), which has the architecture described in Jouvét  
and Cordonnier (2023): 16 two-dimensional convolutional layers each with a  $3 \times 3$  kernel and 32 output filters, with padding  
150 to conserve the frame size, and leaky rectified linear units as the activation functions, resulting in a CNN with about 140 000  
trainable parameters. The CNN has been pretrained on a catalogue of mountain glaciers specifically chosen to be heterogenous  
and representative of a variety of glacier shapes (Jouvét et al., 2022).

The benefit of the CNN approach over that of traditional ice flow models is that evaluation of the pretrained neural network  
is fast, especially on a GPU. Additionally, it allows the use of the Blatter-Pattyn model, which for mountain glaciers is more  
155 appropriate than the SIA used in the Millan global thickness inversion study.



The encoding of the Blatter-Pattyn model equations as a neural network also makes the inversion framework simple to set up, taking advantage of automatic differentiation, and using tools from the Tensorflow (Abadi et al., 2015) and Keras (Chollet, 2015) Python libraries. The aim of the inversion module in IGM is to invert the ice flow mapping (1). We take known surface velocity data, surface topography data, and thickness measurements (where present), and pick some combination of thickness  
 160  $h$ , surface topography  $s$ , Arrhenius factor  $A$ , and sliding coefficient  $c$  to be control variables which we can adjust. The aim is to obtain an optimal fit of these control variables across the whole glacier, in the sense that the misfit between the surface velocity output from the emulator (1) and the observed surface velocity is small (Jouvet, 2023).

In this study, we focus on thickness  $h$  as the only control variable. The optimized map is obtained by minimising the cost function

$$165 \quad \mathcal{J}(h) = \mathcal{C}^u + \mathcal{C}^h + \mathcal{R}^h + \mathcal{P}^h. \quad (2)$$

Letting  $\mathcal{M}$  denote the ice-covered domain, the misfit between modelled and observed surface velocities is

$$\mathcal{C}^u = \frac{1}{2\sigma_u^2} \frac{1}{\text{area}(\mathcal{M})} \int_{\mathcal{M}} |\mathbf{u}_s^{\text{obs}} - \mathcal{N}_\lambda(h, s, A, c)|^2 dm, \quad (3)$$

where  $\mathbf{u}_s^{\text{obs}} = (u_s^{\text{obs}}, v_s^{\text{obs}})$  denotes the vector field of observed horizontal velocity at the surface and  $|\cdot|$  denotes the Euclidean norm. Letting  $\mathcal{T} \subseteq \mathcal{M}$  denote the subset of cells for which thickness observations exist, the misfit between modelled and  
 170 observed ice thickness is

$$\mathcal{C}^h = \frac{1}{2\sigma_h^2} \frac{1}{\#\text{cells} \in \mathcal{T}} \sum_{\text{cells} \in \mathcal{T}} |h - h^{\text{obs}}|^2, \quad (4)$$

where  $|\cdot|$  denotes absolute value. Details of the computation of the discretized  $h^{\text{obs}}$  are given in Sect. 2.2.2.

A regularization term is included to minimize the presence of non-physical small-scale spatial variations in the thickness field. Although our control variable is thickness  $h$ , we instead regularize the bedrock  $b = s - h$  (note that the surface elevation  
 175  $s$ , which is derived from a DEM, does not change at all in our inversion setup, and that  $b = s$  outside  $\mathcal{M}$ ). While the inclusion of this term has the effect of regularizing the ice thickness, it additionally imposes smoothness of the bedrock at the boundary of  $\mathcal{M}$ . The regularization term for the bedrock elevation is

$$\mathcal{R}^h = \frac{\alpha_h}{2\sqrt{\beta}} \frac{1}{\text{area}(\Omega)} \int_{\Omega} \left( |\nabla b \cdot \tilde{\mathbf{u}}_s^{\text{obs}}|^2 + \beta |\nabla b \cdot \tilde{\mathbf{u}}_s^{\text{obs}, \perp}|^2 \right) dm \quad (5)$$

where  $\tilde{\mathbf{u}}_s^{\text{obs}}$  is the observed surface velocity after smoothing with a Gaussian filter with standard deviation 3 and then nor-  
 180 malizing,  $(\tilde{\mathbf{u}}_s^{\text{obs}})^{\perp}$  is the unit vector field orthogonal to it, and  $\beta$  is a coefficient which allows for anisotropic smoothing ( $\beta = 1$  corresponds to isotropic smoothing,  $\beta$  closer to 0 enforces more smoothing in the along-flow direction). In all of our experiments, we fix the anisotropy factor at  $\beta = 0.2$ . The final term is a quadratic penalty term (Nocedal and Wright, 2006, Chapter 17) to enforce non-negative ice thickness and zero thickness outside the ice-covered domain:

$$\mathcal{P}^h = 10^{10} \left( \frac{1}{\text{area}(\Omega \setminus \mathcal{M})} \int_{\Omega \setminus \mathcal{M}} h^2 dm + \frac{1}{\text{area}(\text{cells where } h < 0)} \int_{h < 0} h^2 dm \right). \quad (6)$$



185 The parameters  $\sigma_u, \sigma_h$  are user-defined weights which can be thought of as “confidence levels” for the observed surface velocity and thickness respectively - a lower  $\sigma$  corresponds to more “confidence” and more weight placed on matching these observations. Note that these  $\sigma$  values do not represent measurement error; they are intended to be tuned by the user (Jouvet, 2023). The regularization parameter  $\alpha_h$  controls how much weight is placed on smoothing the thickness field.

The cost  $\mathcal{J}(h)$  is minimized using the Adam optimizer (Kingma and Ba, 2017), which is a popular method for training  
190 neural networks, and is a variation on stochastic gradient descent with momentum. The inversion begins with a pretrained neural network  $\mathcal{N}_\lambda$ , which goes through one iteration of retraining (also with Adam) after each inversion iteration, using the current glacier geometry as the training data. The aim of retraining is to keep the neural network cost (the energy functional associated with the Blatter-Pattyn model) low, so that the emulator continues to produce output that is close to Blatter-Pattyn solutions. Examples of how the inversion cost (Eq. 2) and neural network cost evolve over iterations of the optimization  
195 algorithm in practice can be found in Appendix A.

## 2.2 Data

### 2.2.1 Data acquired through OGGM

To retrieve the required data, we use the built-in framework of IGM, which in turn relies on preprocessed data provided by the Open Global Glacier Model (OGGM) developed by Maussion et al. (2019). OGGM defines a spatial grid for each glacier with  
200 a resolution of  $H = 100$  m. All variables are projected onto this grid.

Glacier outlines and identification numbers are provided by the Randolph Glacier Inventory (RGI) v6.0 (RGI Consortium, 2017). A rasterized mask is created from the outline to define ice-free areas. The digital elevation model (DEM) is that of Copernicus (2019), with acquisition dates between 2010 and 2015. Surface velocities are those computed by Millan et al. (2022), derived by feature tracking of image pairs acquired by the optical sensors onboard satellites Landsat 8 and Sentinel-2,  
205 and the synthetic aperture radar onboard Sentinel-1, between 2017 and 2018. Finally, to initialize the IGM inversion, we use the ice thickness estimate from Millan et al. (2022), which was derived from the velocity dataset from the same study.

### 2.2.2 Thickness observations

In addition to the data available through OGGM, we use the thickness observations from Pritchard et al. (2026). These measurements, obtained by airborne ground-penetrating radar in October and November 2019, cover 13 glaciers (as identified in  
210 RGI v6.0) near Mount Everest. Further details on the processing of the radar data, as well as error analysis, are available in Pritchard et al. (2026).

The pointwise thickness measurements are provided in a vector (ESRI shapefile) format. In some places, points are as close together as 1 m, while the resolution of our model is 100 m. We rasterize the thickness observations for use in IGM by taking the mean thickness in a  $100 \text{ m} \times 100 \text{ m}$  square centred on each coordinate point in our grid.

215 We acknowledge that the aggregation of thicknesses in this way does incur a loss of information from the original vector dataset. While it would in theory be possible to compare the modelled thickness field with pointwise thickness measurements,

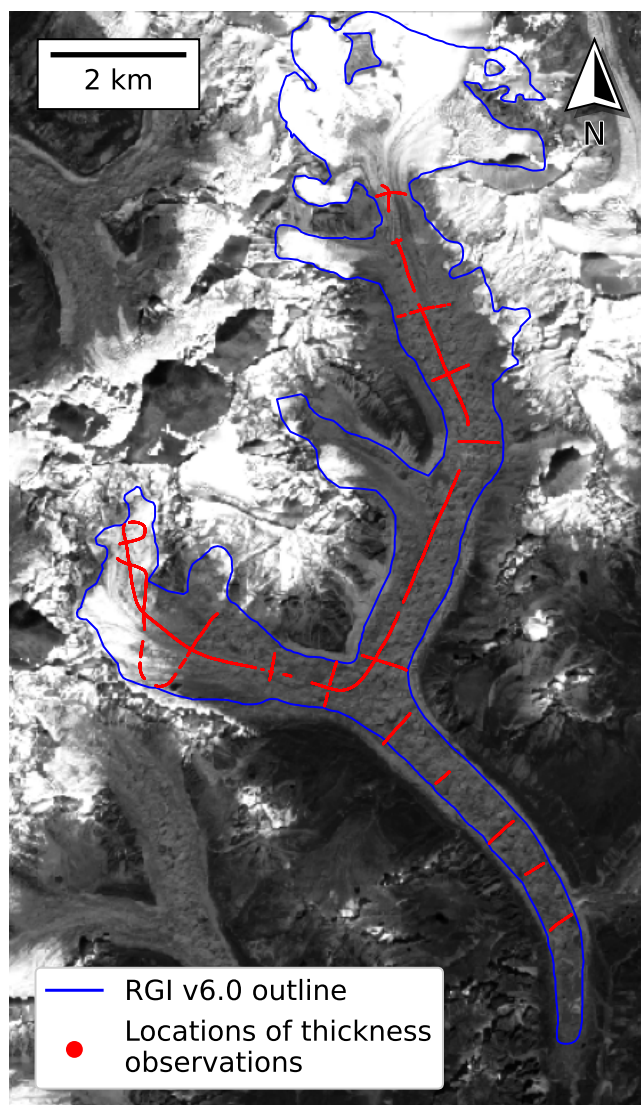


**Figure 1.** Bhote Kosi glacier (RGI60-15.03422) outline in blue. Locations of Pritchard et al. (2026) thickness observations in red. Background image is a Sentinel-2 scene (band 04) from 15 October 2019 (contains modified Copernicus Sentinel data [2019] processed by Sentinel Hub).



as recommended by Nixon-Hill et al. (2024), this would require refactoring of the IGM code, and we would instead be faced with the question of how to interpolate the modelled thickness field at the observation locations. We opt for rasterization of the thickness dataset, as this is easily implemented within the current IGM framework and a similar approach was taken in  
220 Farinotti et al. (2021).

The glacier outlines from RGI v6.0 are intended to represent the state of the glacier in the year 2000 (or as close as possible), and comparison with more recent high-resolution satellite imagery shows that there are cases where an outline may not be representative of the recent state of the glacier. Indeed, when preparing the thickness observation data, it became clear that some thickness observations lie outside RGI v6.0 glacier outlines (see e.g. Fig. B1). For ease of modelling, we prioritise the  
225 outlines over the observations, and discard all thickness observations outside the rasterized glacier mask derived from the outline.

### 2.3 Methodology

Bhote Kosi glacier (whose RGI v6.0 ID is RGI60-15.03422) was chosen for an in-depth study. It is one of the largest glaciers in the Pritchard et al. (2026) dataset, and has good coverage of thickness observations, with several longitudinal (along-flow) and  
230 across-flow profiles, and observations across a wide elevation range (see Fig. 1). Pritchard et al. (2026) notes that different parts of this glacier are known by different names: Bhote Kosi is the southern main “trunk” of the glacier, with the west tributary and north tributary called Lunag and Nangpa respectively. Throughout this paper we typically use the name Bhote Kosi to refer to the entire glacier, since it is dynamically connected and appears as one glacier in RGI v6.0.

We perform several thickness inversion experiments on Bhote Kosi glacier, starting with a simple configuration, and progressively introducing more complexity. We begin by performing inversions without calibrating to thickness observations, in order  
235 to tune the ratio between  $\sigma_u$  and  $\alpha_h$ . We then introduce thickness observations into the inversion, aiming to find an appropriate value for  $\sigma_h$ , and performing cross-validation experiments to explore the value added by calibrating to thickness observations.

Initial experiments with IGM inversion showed that the choice of parameters  $\sigma_u$ ,  $\sigma_h$  and  $\alpha_h$  can have a significant effect on the resulting thickness field (see Fig. C1). With our in-depth study on Bhote Kosi, we aim to find a set of parameters that  
240 provide an optimal balance between matching observed surface velocities and producing a realistically smooth thickness field.

#### 2.3.1 Error metrics

In each experiment, we measure the error with unseen (validation) thicknesses using two different statistics: the mean absolute error (MAE) and the mean bias error (MBE). The MAE over a set of grid cells  $\mathcal{T}$  with thickness observations is the absolute value of the difference between modelled and observed thickness, averaged over all cells in  $\mathcal{T}$ :

$$245 \text{MAE}(\mathcal{T}) = \frac{1}{\#\text{cells} \in \mathcal{T}} \sum_{\text{cells} \in \mathcal{T}} |h - h^{\text{obs}}|. \quad (7)$$



The MBE over a set of grid cells  $\mathcal{T}$  is simply the difference between modelled and observed thickness, averaged over all cells with a thickness observation:

$$\text{MBE}(\mathcal{T}) = \frac{1}{\#\text{cells} \in \mathcal{T}} \sum_{\text{cells} \in \mathcal{T}} (h - h^{\text{obs}}). \quad (8)$$

By including the sign of the difference, the MBE has a convenient interpretation: a negative MBE indicates that on average, the model underestimates the ice thickness (and hence the total volume), whereas a positive MBE indicates overestimation. It is desirable for both MAE and MBE to be close to zero.

### 2.3.2 “Velocity-only” inversion

We begin by matching observed velocities only (the term  $\mathcal{C}^h$  is omitted from (2)). Available thickness observations are used only as validation data, i.e. to assess the accuracy of the thickness estimate after the inversion has been performed. We use IGM’s default values of  $A = 78 \text{ MPa}^{-3} \text{ yr}^{-1}$  for the Arrhenius parameter and  $c = 0.0464 \text{ MPa yr}^3 \text{ m}^{-3}$  for the sliding coefficient (both are taken to be spatially constant). The velocity-only inversion scheme was run for 18 approximately logarithmically spaced values of  $\alpha_h$  between 0.01 and 60, keeping  $\sigma_u = 1$  fixed (note that we can fix one of the coefficients without loss of generality: multiplying all cost terms by the same factor would not change the locations of minima). For each  $\alpha_h$ , the optimization algorithm was run for 1000 iterations, resulting in a different final thickness field each time.

The lower the value of  $\mathcal{R}^h$ , the smoother the thickness field. Likewise, a relatively lower value of  $\mathcal{C}^u$  corresponds to closer agreement with observed surface velocities. Since in general it will not be possible to minimize both quantities simultaneously, we attempt to find a value of  $\alpha_h$  which balances the effects of the two terms, ensuring a close fit to observed surface velocities, yet also an acceptably smooth thickness field with few small-scale non-physical artefacts. The values of  $\mathcal{C}^u$  and  $\mathcal{R}^h / \alpha_h$  at the final iteration were recorded and plotted against each other on a scatter plot with a log-log scale, following the “L-curve” technique (Hansen and O’Leary, 1993).

### 2.3.3 Cross-validation of thickness constraints

We then introduce observed thickness measurements into the inversion, so that the cost function is as presented in (2), matching observed velocities and thicknesses simultaneously.

Constraining to thickness observations at some locations does not guarantee accurate modelled thickness at unconstrained locations. To evaluate the effect of thickness constraint on unconstrained locations, we perform non-exhaustive cross-validation experiments. In each experiment, available thickness observations are partitioned into a calibration set, whose cells appear in the thickness mismatch cost term  $\mathcal{C}^h$ , and a validation set, whose cells are used only after the inversion to estimate the error on unseen data, using the statistics described in Sect. 2.3.1. The wide spatial range of thickness observations available for Bhote Kosi glacier and the resulting range of choices for partitioning the data allows us to gain a variety of information from these experiments.

Points belonging to each thickness observation profile shown in Fig. 1 were manually labelled. The calibration and validation sets were then chosen following the methodology of a subset of the experiments from Farinotti et al. (2021). After fixing the



regularization parameter  $\alpha_h$ , we perform inversions where the calibration set is biased in four different ways, mimicking scenarios which often occur in glacier thickness surveys due to limitations associated with fieldwork: observations only in the 280 thickest parts of the glacier, observations only in the flattest parts of the glacier, observations only in the lowest elevations, and longitudinal (along-flow) profiles only.

The aim of these experiments is to assess the effect of the parameter  $\sigma_h$  on the inversion, and ideally to determine a value of  $\sigma_h$  that provides a good fit to thicknesses in the calibration set while avoiding overfitting. In other words, the error on the calibration set should be low, and the error on the validation set should not be too high. We investigate whether there is a value 285 of  $\sigma_h$  that is suitable for all four of the calibration sets considered here. A set of 21 approximately logarithmically spaced values for  $\sigma_h$  between 1 and  $10^5$  are considered.

### 2.3.4 Sensitivity of inversion to Arrhenius parameter

The Arrhenius parameter is a parametrization of viscosity based on Glen's flow law (Glen, 1953), a simple power law that is convenient to use, but does not capture every detail of glacial rheology. Its true value is difficult to measure in the field, and 290 can depend on several factors such as ice temperature, water content, grain size, and impurities (Cuffey and Paterson, 2010). Intuitively, a lower  $A$  corresponds to colder, stiffer ice.

In all of our previous experiments, we used the IGM default values of  $A = 78 \text{ MPa}^{-3} \text{ yr}^{-1}$  for the Arrhenius parameter and  $c = 0.0464 \text{ MPa yr}^3 \text{ m}^{-3}$  for the sliding coefficient. Optimizing both physical parameters simultaneously may be an ill-posed problem, as a high surface velocity could be equally explained by a high  $A$  (corresponding to warmer, less viscous ice) or a 295 low  $c$  (corresponding to more basal sliding). Therefore we fix  $c$  and perform sensitivity analysis on the Arrhenius parameter only.

We run velocity-only inversions (with all available thickness profiles acting as the validation set), with the regularization parameter  $\alpha_h$  fixed, for seven equally spaced values of the Arrhenius parameter  $A$  between 13 and  $91 \text{ MPa}^{-3} \text{ yr}^{-1}$ . We consider different metrics to determine an optimal value for  $A$ : which  $A$  value matches velocities best (low  $C^u$ ), or which  $A$  300 value matches unseen thicknesses best (small MAE/MBE on validation set). We record the surface velocity cost  $C^u$ , MAE, and MBE at the final iteration.

## 3 Results

### 3.1 Velocity-match-only inversion

Following the experiment described in Sect. 2.3.2, Fig. 2(a) plots the final values of  $C^u$  against  $\mathcal{R}^h/\alpha_h$ , and a clear "L" shape 305 is seen. Heuristically, values of  $\alpha_h$  close to the "corner" of the L-curve provide a good compromise between minimal velocity mismatch and low spatial variability in the thickness field. Here we find that  $\alpha_h = 6, 10$  lie in this region, and are therefore considered acceptable by this method.

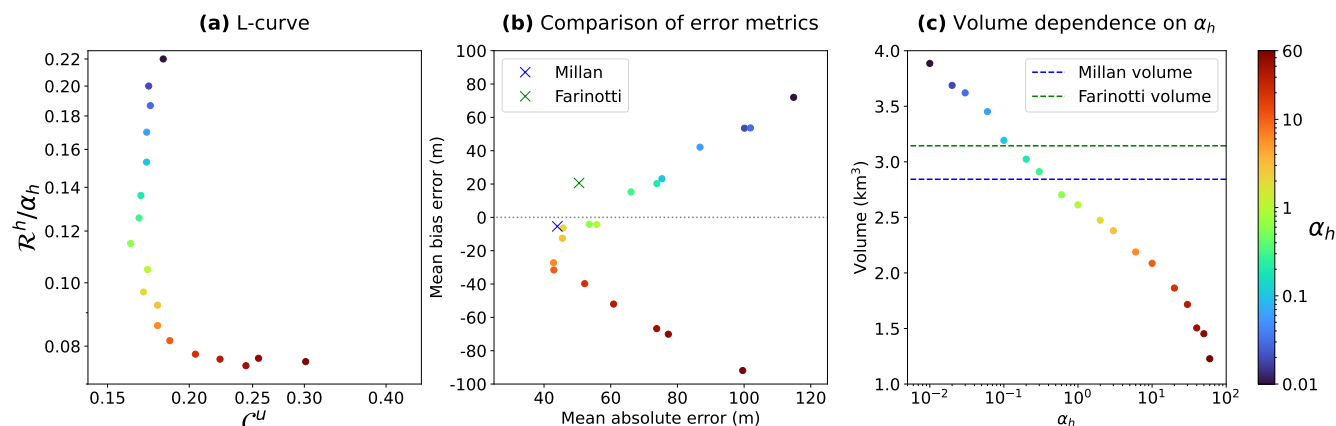


**Figure 2.** In each figure, each coloured point represents a unique value of  $\alpha_h$  and its resulting thickness field. (a) L-curve relationship between  $C^u$  and  $\mathcal{R}^h$ . (b) Relationship between MAE and MBE. (c) Relationship between  $\alpha_h$  and total volume.

During this experiment, we also measured the MAE and MBE between our final thickness field and the observed thicknesses. We found that the lowest MAE values (between 42 m and 46 m) were achieved for  $\alpha_h = 2, 3, 6, 10$  (Fig. 2(b)), including values which were, incidentally, also found in the corner of the L-curve. The MBE values closest to zero (between  $-4$  m and  $-7$  m) are achieved for  $\alpha_h = 0.6, 1, 2$ ; however, the resulting thickness fields are visibly under-regularized compared to those achieved for higher values of  $\alpha_h$  (e.g. Fig. C1(b)). Additionally, the thickness fields for  $\alpha_h = 0.6, 1$  show poorer accuracy in terms of MAE than the thickness fields for  $\alpha_h = 6, 10$ . Figure 2(b) also demonstrates clearly that MAE and MBE need not be minimized simultaneously: the value of  $\alpha_h$  producing the lowest MAE is not the same as the  $\alpha_h$  with the lowest MBE.

315 Additionally worth noting is that the value of  $\alpha_h$  appears to have a direct effect on the volume of the modelled glacier, with lower  $\alpha_h$  corresponding to a higher final volume (Fig. 2(c), Fig. C1), possible reasons for which are discussed in Sect. 4.1.

Based on the results found here, we acknowledge that there is no single optimal value of  $\alpha_h$ , and valid arguments could be made for choosing any one of  $\alpha_h = 2, 3, 6, 10$ . We use the value  $\alpha_h = 6$  in all of the following experiments.

### 3.2 Cross-validation of thickness constraints

320 Figures 3(a–d) show the profiles chosen for each experiment described in Sect. 2.3.3. Figures 3(e–h) show the MAE against  $\sigma_h$ , for each of the four cross-validation experiments. In all four experiments, the error on the calibration set decreases as the strength of thickness constraint is increased (by decreasing  $\sigma_h$ ). For all four experiments, the MAE on the calibration set drops below 10 m for any  $\sigma_h \leq 300$ , and is very small for any  $\sigma_h \leq 100$ . On the other hand, there does not appear to be a clear relationship between the value of  $\sigma_h$  and the validation set error, which remains between 32 m and 45 m for all four experiments and all values of  $\sigma_h$ .

Figure 4 shows the resulting thickness maps when constraining to no profiles (i.e. the velocity-only result), all available profiles, low-elevation profiles only and longitudinal profiles only.

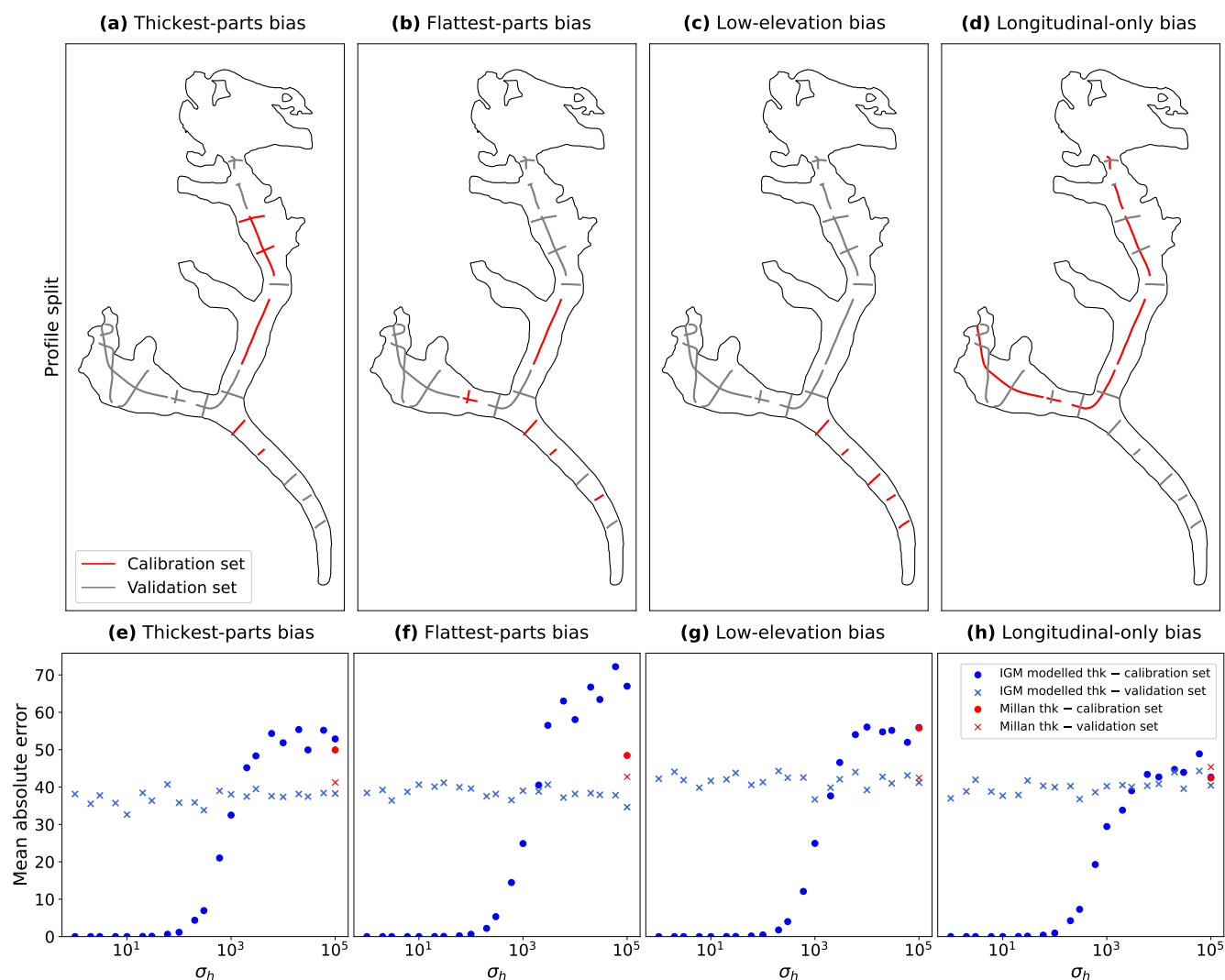


**Figure 3.** (a–d): partitions of thickness observations on Bhote Kosi into calibration and validation sets, with red and grey lines representing profiles in the calibration set and validation set respectively. (e–h): mean absolute error of modelled vs observed thickness against  $\sigma_h$  for the above choice of calibration set. Blue markers denote the MAE in IGM thickness estimates at locations in the calibration and validation set. Red markers denote the MAE in the Millan thickness estimate at locations in the calibration and validation set. Circles and crosses denote the MAE on the calibration and validation set respectively.

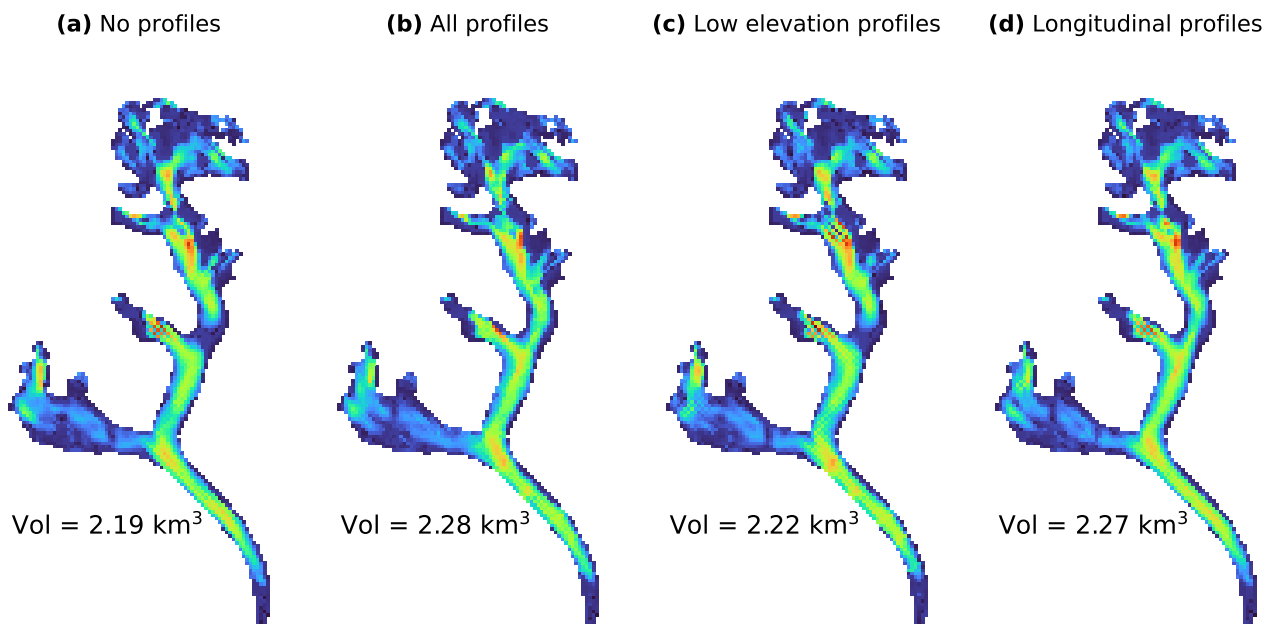


**Figure 4.** Thickness maps produced by IGM, obtained by constraining to (a) no thickness profiles, (b) all thickness profiles, (c) the low-elevation profiles highlighted in Fig. 3(c), (d) the longitudinal profiles highlighted in Fig. 3(d). In all cases the regularization parameter was  $\alpha_h = 6$  and the thickness confidence parameter was  $\sigma_h = 300$ . The colour scale for all panels is identical to that of Fig. 6(a,b).

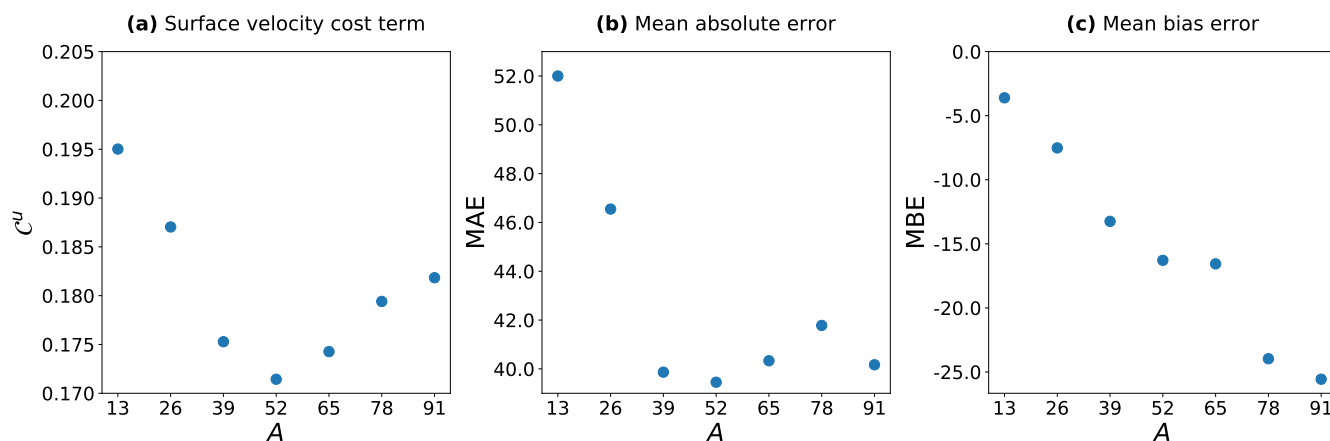


**Figure 5.** (a) Surface velocity cost term  $C^u$  (Eq. (3)) against Arrhenius parameter  $A$ , (b) MAE against  $A$ , and (c) MBE against  $A$ .



### 3.3 Sensitivity of inversion to Arrhenius parameter

The results of the experiment described in Sect. 2.3.4 are presented in Fig. 5. In Fig. 5(a), we find that the lowest surface velocity cost is found for  $A = 52 \text{ MPa}^{-3}\text{yr}^{-1}$ , but that there is only a modest reduction of around 4.5% in surface velocity cost against the result for  $A = 78 \text{ MPa}^{-3}\text{yr}^{-1}$ . Figure 5(b) shows that the lowest mean absolute error is achieved for  $A = 52 \text{ MPa}^{-3}\text{yr}^{-1}$ , but that the mean absolute errors for the results for  $A$  between 39–91  $\text{MPa}^{-3}\text{yr}^{-1}$  are all very close, lying between 39 m and 42 m.

In Fig. 5(c), we see that the mean bias errors are negative for any  $A$  value. This is, however, consistent with our results from Fig. 2(b) showing that the mean bias error is negative for  $\alpha_h = 6$ . In general, increasing  $\alpha_h$  has the effect of lowering the volume, whereas decreasing  $A$  corresponds to colder, stiffer ice, resulting in a higher volume (since a higher thickness is required to “explain” the same velocity). Low  $A$  values in this experiment are likely counteracting the choice of  $\alpha_h$  which already resulted in a negative MBE (indicative of an underestimation of the glacier volume). The mean bias error closest to zero is achieved for  $A = 13 \text{ MPa}^{-3}\text{yr}^{-1}$ , but since this value also produces a very high mean absolute error, there is insufficient evidence to recommend this value.

## 4 Discussion

### 4.1 Effect of regularization parameter

We initially endeavoured to produce the “best possible” thickness field with velocity data only, by making a careful choice of the regularization parameter  $\alpha_h$ , guided by the L-curve analysis in Sect. 3.1.

It is clear from our results that the choice of regularization parameter  $\alpha_h$  has a strong effect on the final volume of the modelled glacier (Figs. 2(c), C1). To understand why this is the case, observe that the regularization term (Eq. 5) is non-negative, and reaches zero if and only if  $\nabla b = 0$  everywhere in  $\Omega$ , i.e. when the bedrock elevation  $b$  is constant. Although the value of  $b$  does not change outside the glacier mask  $\mathcal{M}$ , flattening the bedrock inside  $\mathcal{M}$  and attempting to match the bedrock elevation at the boundary of  $\mathcal{M}$  will still reduce the regularization cost. In addition, the penalty term (Eq. 6) enforces zero thickness outside  $\mathcal{M}$ . These two effects together encourage low ice thickness  $h$ . This thinning effect is stronger when the regularization term  $\mathcal{R}^h$  is larger in comparison to the other terms in Eq. 2, i.e. when  $\alpha_h$  is larger. Hence, increasing the value of  $\alpha_h$  results in a decrease in modelled volume. Although this effect is somewhat undesirable, inclusion of a regularization term is nonetheless necessary to avoid non-physical small-scale spatial variations in the thickness field (as seen in e.g. Fig. C1(a,b)).

### 4.2 Artefacts in thickness field

We observe in Fig. 6(b) that in the IGM estimate, there is an area of very low thickness present about halfway up the north tributary of the glacier, coinciding with a location where measured velocities are low (Fig. 7(a)). Small ice velocities are known to have high relative errors due to limitations associated with feature tracking methods (Dehecq et al., 2019). Since the ice is observed as almost stationary, there is insufficient information to infer the ice thickness from the surface velocity at



this location. A similar issue may also be present at the area near the glacier terminus, as we also observe low velocity and  
360 low modelled thickness there. Despite using the same surface velocities from which the Millan estimate was derived, these  
low-thickness features were not present in the Millan estimate (Fig. 6(a)). This phenomenon was also observed on preliminary  
inversions of Ngozumpa and Lumsamba glaciers (not shown); however, although those glaciers are well-surveyed, we do not  
have sufficient thickness measurements for validation at the affected locations.

Another non-physical artefact visible in the resulting thickness field (Fig. 6(b)) is checkerboarding, which is particularly  
365 apparent in the tributary halfway up the north tributary of the glacier, immediately to the west of the “low-velocity” area. This  
artefact is likely the result of the approximation of spatial gradients with simple finite differences in the cost function, which  
can produce undesirable modes. Further work is required to address this issue within IGM. In the present case, we found that  
this artefact was triggered most severely in a region showing discontinuity in the input velocity field, and vanishes when using  
smoothed data (Appendix D).

### 370 4.3 Error in velocity-only estimate and comparison with Millan estimate

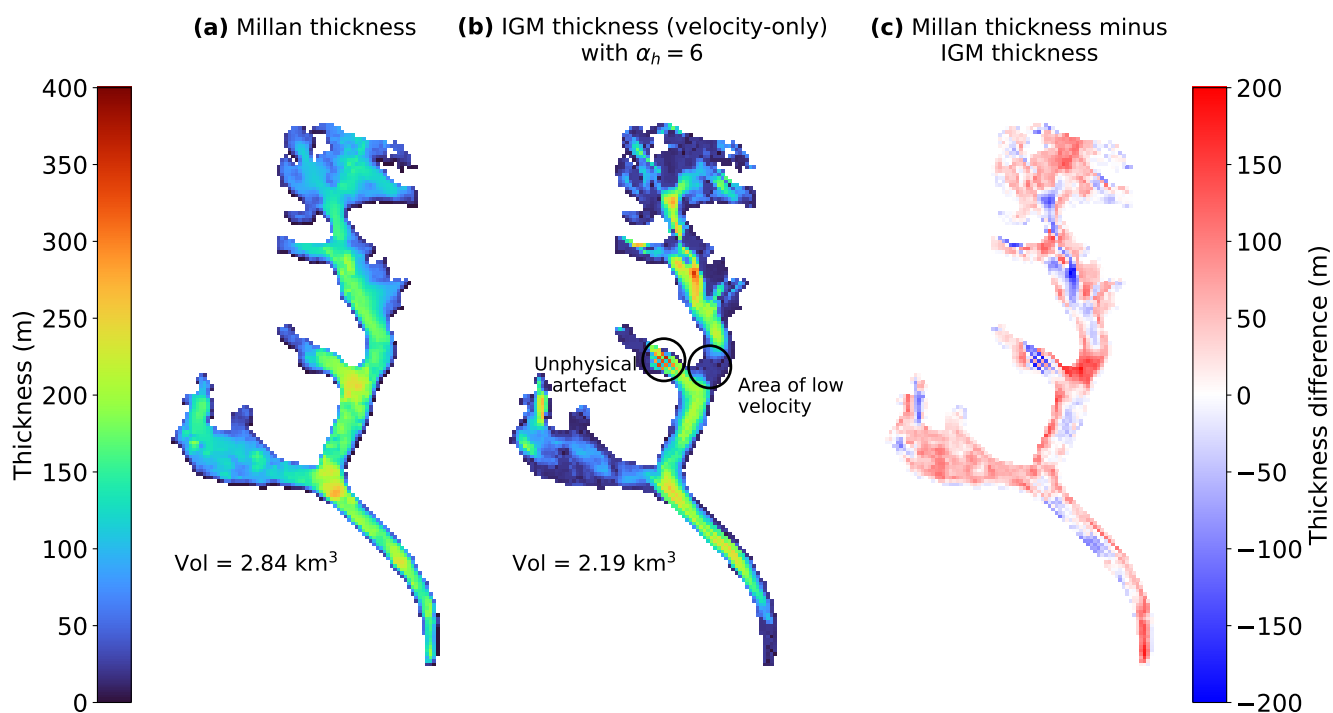


**Figure 6.** (a) The Millan thickness estimate of Bhote Kosi glacier, (b) the IGM velocity-only thickness estimate with the thickness regularization parameter set to  $\alpha_h = 6$ , and (c) the difference between the two.

In our velocity-only inversion, we succeeded in making a reconstruction of the thickness field with errors comparable to the Millan estimate by using surface velocity data only. The observed thickness data (which was not available at the time the

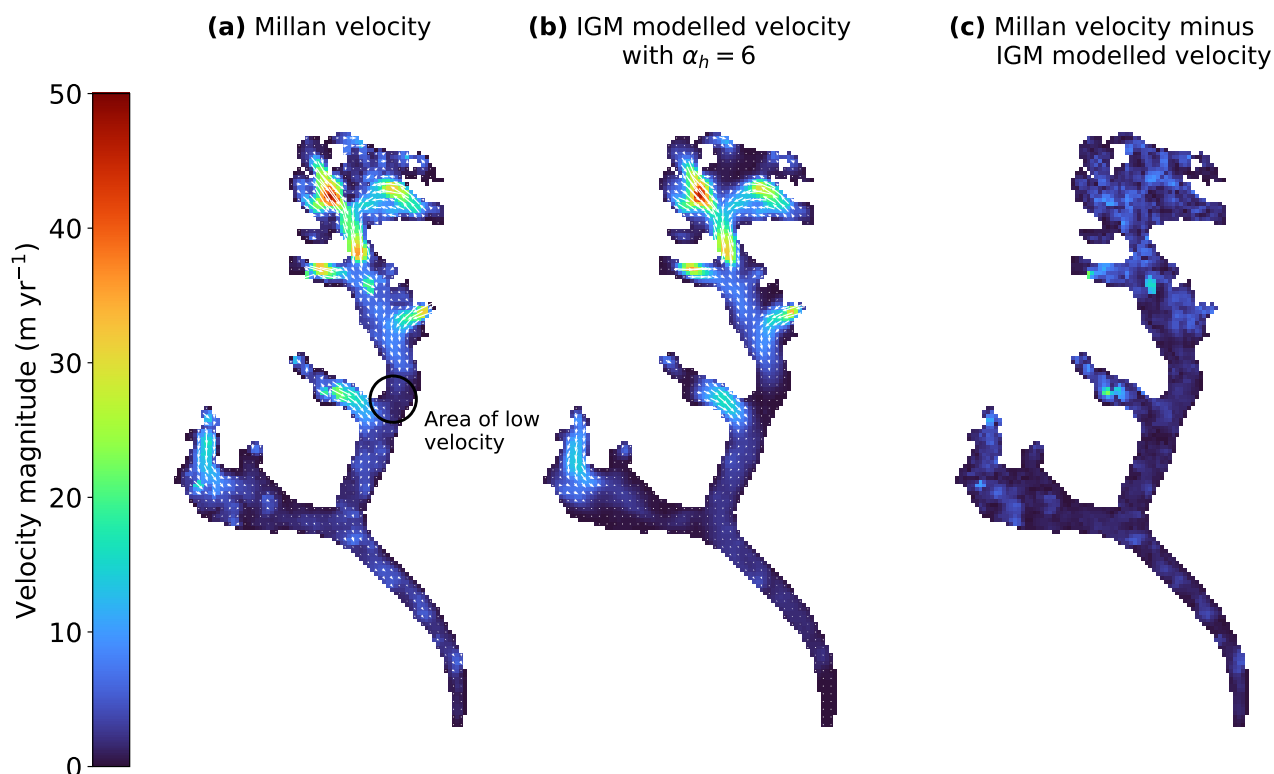


**Figure 7.** (a) The Millan velocity field of Bhote Kosi glacier, (b) the IGM modelled velocity field with the thickness regularization parameter set to  $\alpha_h = 6$ , and (c) the magnitude of the difference between the two.

Millan estimate was published) was valuable in this experiment to validate the results, as otherwise, we would have had no way of validating the accuracy of our results, or indeed the Millan estimate. While it is not appropriate to consider the difference  
375 between our velocity-only thickness estimate and that of Millan et al. (2022) as an “error”, as neither study represents the ground truth, it is of interest to compare the two results, as both attempt to estimate glacier thickness based on the same surface velocity data, without using observed thickness.

Interestingly, in Fig. 8, we observe that IGM produces a more accurate representation of the thickness of the west tributary as compared to the Millan estimate. Measurements show that the west tributary is significantly thinner than the main trunk and north tributary, a detail that is reproduced by IGM even when it is given no direct information about the thickness in this  
380 location. Furthermore, Millan generally overestimates thickness in the west tributary, while underestimating thickness in the rest of the glacier. Improvements by IGM over the Millan study may be due in part to higher-order physics, since IGM is based on the Blatter-Pattyn model, while Millan used the SIA, which excludes stress components which are non-negligible in mountain glaciers.

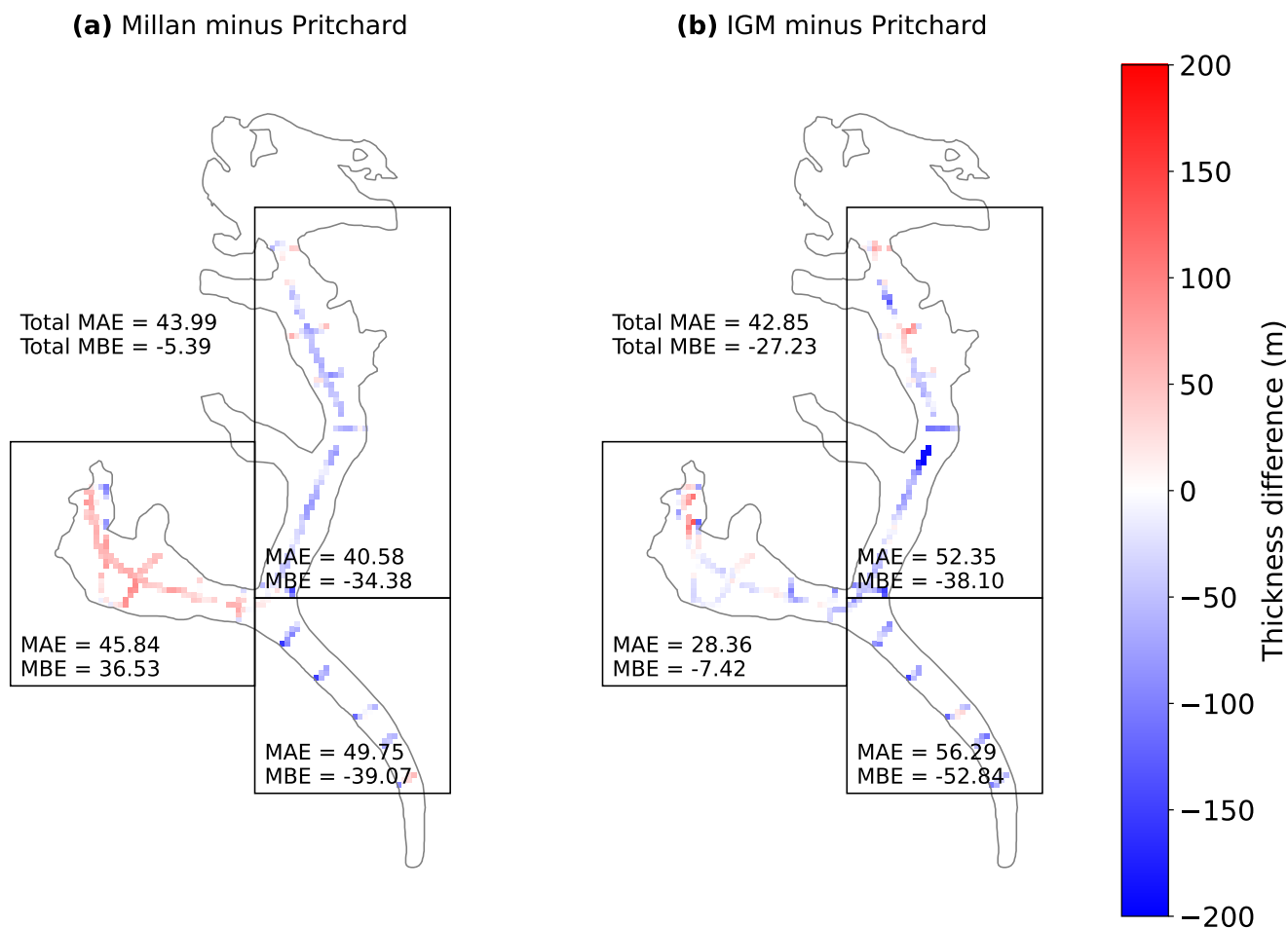


**Figure 8.** (a) The difference between the Millan thickness estimate and the rasterized thickness observations from Pritchard et al. (2026), and (b) the same for the IGM velocity-only ( $\alpha_h = 6$ ) thickness estimate. Bhote Kosi glacier is split into three regions and the MAE and MBE of each model is shown for each region.

385 The IGM-inverted thickness exhibits poorer accuracy in the north tributary as compared to Millan, an error which can be attributed in part to the underestimation of the thickness at the low-velocity area discussed in Sect. 4.2. We observe also that both Millan and IGM underestimate the thickness of the main trunk of Bhote Kosi (Fig. 8).

Pritchard et al. (2026) compared their observed thicknesses with the Millan and consensus estimates, finding that both estimates are biased, with errors of over 100 m in places. In our velocity-only inversions, no value of  $\alpha_h$  succeeded in bringing the MAE below 42 m (Fig. 2(b)), indicating that significant bias is also present in our estimated thickness field. Relative errors (not shown) are over 50% in several places, and over 100% in a handful of locations. Such biases undermine the efficacy of these thickness products when predicting the evolution of a glacier over time. In the case of IGM, the systematic underestimation

390



of thickness may result from the implementation of the regularization term (as discussed in Sect. 4.1). Additionally, although IGM is based on the Blatter-Pattyn model, which contains higher-order stress terms that are missing from the SIA as used by  
395 Millan, it is still not a full-Stokes model. The use of a neural network as an emulator for the Blatter-Pattyn model, rather than a true solver, may also compromise IGM's accuracy, although high-fidelity results have been achieved previously (Jouvet and Cordonnier, 2023).

#### 4.4 Physically consistent ice thickness

Inter-comparison exercises (Farinotti et al., 2017, 2021) focus on assessing the quality of thickness estimates by error with  
400 unseen measured thickness, but one can also consider a high-quality thickness estimate as one which yields an ice velocity field which is consistent with both data and physics. Although our velocity-only IGM thickness estimate is of comparable accuracy to Millan's thickness estimate when considering MAE or MBE across all measured thicknesses over the entire glacier, it does have the additional benefit of higher-order physical consistency between modelled thickness and satellite-observed velocity data. IGM achieves this by enforcing low misfit between modelled and observed surface velocity (Eq. 3) during the thickness  
405 optimization.

#### 4.5 Cross-validation and interpolative power of thickness constraints

In Fig. 3, we observe that increasing the strength of the thickness misfit term (Eq. 4) effectively reduces the MAE on the calibration set, but does not reduce the MAE on the validation set. The MAE on the validation set remains between 32 m and  
410 42 m for all four partitions of the data and all values of  $\sigma_h$ , showing at best a modest reduction from the MAE of more than 42 m achieved when omitting thickness profiles from the inversion (Sect. 3.1). This indicates that the thickness observations have limited interpolative power in this model setup, i.e. constraining to thickness observations has only a weak effect on the accuracy of the modelled thickness at unconstrained locations. This is further confirmed by Fig. 4, which shows the resulting thickness map when taking  $\sigma_h = 300$  and constraining to different subsets of the available thickness profiles. We see that the thickness distribution constrained to all profiles (Fig. 4(b)) appears largely the same as that obtained without thickness  
415 constraints (Fig. 4(a)), with only local-scale changes visible in the resulting thickness map, and a small increase in total volume. We observe also that between the thickness maps obtained by constraining to low-elevation profiles (Fig. 4(c)) and longitudinal profiles only (Fig. 4(d)), the calibration sets in these two cases have no profiles in common and no intersection between profiles in the two sets. Both thickness fields look very similar to the velocity-only thickness field at locations without observations.

420 While this result indicates that overfitting to observed thicknesses is not an issue, it also indicates that constraining to thickness observations has little effect on the thickness at unconstrained locations with this modelling approach. A potential reason for the low interpolative power of thickness observations is the limited spatial influence of stress perturbations according to the Blatter-Pattyn stress balance. Changes in speed and driving stress are felt over the membrane length scale (Robinson et al., 2022), typically on the order of a few ice thicknesses. In the present context, consider a location where there are no  
425 thickness constraints. If a thickness constraint is introduced close by, this will influence velocities at the location, and the



optimization therefore will need to adjust thickness at the location in order to reduce the misfit with observed surface velocities. If the introduced thickness constraints are sufficiently far away, the influence on velocity is minimal, and therefore so is the adjustment. With strong enough regularization, there could be a smoothing length scale that is larger than the membrane length scale, leading to non-physical interpolation of thickness constraints.

430 The disappearance of the erroneous low-thickness zone in the north tributary when adding thickness constraints (compare Figs. 4(a, b)) highlights the importance of constraining to thickness profiles where available, as in this case their inclusion was able to correct for a lack of information from the surface velocity data.

#### 4.6 Arrhenius parameter

IGM's default value for  $A$  is  $78 \text{ MPa}^{-3}\text{yr}^{-1}$ , which heuristically corresponds to temperate glaciers around  $0 \text{ }^\circ\text{C}$  (Cuffey  
435 and Paterson, 2010, Table 3.4), and may not be optimal for glaciers in HMA. On the other hand, the value used by Millan for glaciers in the Everest area was  $13 \text{ MPa}^{-3}\text{yr}^{-1}$ , which was based on a very small number of thickness observations for glaciers elsewhere in HMA. Their value approximately corresponds to between  $-5$  and  $-10 \text{ }^\circ\text{C}$  (Cuffey and Paterson, 2010, Table 3.4), colder than measured englacial temperatures on nearby Khumbu glacier (Miles et al., 2018). Indeed, the use of different values of  $A$  may partially explain why Millan's modelled volume is slightly higher than ours (Fig. 6): when directly  
440 estimating thickness via the SIA (Millan et al., 2022, Eq. 2), there is an inverse relationship between  $A$  and ice thickness.

We acknowledge that using a different Arrhenius value for our previous experiments may change our results slightly (Fig. 5), but we did not identify an ideal value. If we were to switch to a different (spatially constant) value of  $A$ , the aspect of our result that would be most affected would be the glacier volume (Fig. 5(c)). However, changing  $A$  would be unlikely to affect our earlier conclusions: that the regularization parameter  $\alpha_h$  affects the volume and can be optimized with L-curve analysis,  
445 and that tuning the thickness confidence parameter  $\sigma_h$  reduces the error at locations with thickness observations seen by the model, but seems to have little effect on unseen thickness observation locations. Future work could consider spatially varying  $A$ , a scenario which is more realistic since englacial temperatures (and therefore  $A$ ) may vary throughout a glacier.

#### 4.7 Applicability to other glaciers

Our results demonstrate that a lack of thickness observations need not be a barrier to producing a reasonable thickness estimate,  
450 as we were able to produce results with estimated accuracy comparable to the leading thickness estimates by constraining to surface velocity data alone, by making an informed choice for the regularization parameter  $\alpha_h$ . Although our results showed that significant bias was present in non-thickness-constrained results, and that thickness constraints introduced only limited changes to the thickness at unconstrained locations, results on other glaciers may vary.

For a glacier with no thickness observations (which is the case for most glaciers), it would not be possible to create a plot  
455 equivalent to Fig. 2(b). Regardless, it would still be possible to create an L-curve plot similar to Fig. 2(a), and, assuming the desired L-shape is present, choose a value in the corner of the L (indeed, for this example we could have chosen the value  $\alpha_h = 6$  based on this alone). In our example, the  $\alpha_h$  values in the corner of the L-curve also gave a low MAE. It would also be possible to compare the total volume with the consensus and Millan total volumes, as in Fig. 2(c): while neither of these



studies represent the ground truth, this comparison serves as a consistency check to flag up any thickness fields whose volume  
460 deviates implausibly from other estimates.

Preliminary inversions were performed on the other 12 glaciers (as outlined in RGI v6.0) with thickness observations from  
Pritchard et al. (2026). The parameters found to be optimal for Bhote Kosi were used ( $\alpha_h = 6$ ,  $\sigma_h = 300$ ), with results (not  
shown) varying in quality. Very low modelled volume was observed for multiple glaciers, particularly smaller glaciers where  
a resolution of 100 m may not be fine enough to resolve physical details. This demonstrates that the parameters, particularly  
465  $\alpha_h$ , may be somewhat glacier-dependent. We note that the term  $C^u$  (Eq. 3) involves a mean over the glacier mask  $\mathcal{M}$ , but  $\mathcal{R}^h$   
(Eq. 5) involves a mean over the rectangular domain  $\Omega$ . When switching to a different glacier, the ratio between the areas of  
 $\mathcal{M}$  and  $\Omega$  is likely to be slightly different. This is one factor that may affect the regularization parameter required. In order to  
produce accurate thickness maps for other glaciers, a full L-curve analysis per glacier would likely be beneficial. A finer spatial  
resolution may also be required for smaller glaciers.

#### 470 **4.8 Recommendations for observation locations**

Farinotti et al. (2021) found that it is advisable not to have all thickness observations concentrated at the lowest elevations of  
the glacier, and that covering the thickest parts (which often coincide with the flattest parts) is the most effective way to ensure  
accurate volume estimation.

Our investigation demonstrated that there is a lack of “signal” from low-velocity locations, which often leads to erroneous  
475 low modelled thickness, as thin ice can also yield a similar near-stagnant ice flow. This effect can be corrected by the inclusion  
of a thickness profile for calibration. We therefore propose, in addition to the above considerations from Farinotti et al. (2021),  
that fieldworkers should aim to measure the thickness at such low-velocity areas, because this may be the best way to ensure  
accuracy at those locations when estimating thickness.

Conversely, thickness observations are also valuable in fast-flowing locations, since this is where velocity inversions are most  
480 effective. In such locations, thickness observations can aid in model-parameter optimisation, i.e. the choices of  $\alpha_h$  and  $A$  in  
our setup. Furthermore, the membrane length scale is longer where there is faster ice flow, thereby increasing the interpolative  
power of thickness observation.

Following the discussion in Sect. 4.5, we reiterate that the inclusion of thickness constraints does not guarantee improved  
estimates of thickness at distant locations. Therefore, in our setup, the calibration of ice thickness at locations with no nearby  
485 measurements relies heavily on making optimal choices for the model parameters  $\alpha_h$  and  $A$ .

## **5 Conclusions and further work**

In this study, we used IGM’s higher-order (as compared to previous thickness estimation methods) inversion capabilities to  
produce glacier ice thickness estimates that are physically consistent with surface velocity data, exploring methods for choosing  
inversion parameters. By leveraging a novel dataset of glacier thickness observations, we were able to compare results obtained  
490 by additionally constraining to observed thicknesses.



When constraining to surface velocities only, we found that the accuracy of the resulting thickness field depends strongly on the choice of the thickness regularization parameter, with a suboptimal choice resulting in poor agreement with true thickness, and a potentially inaccurate total volume. Furthermore, the thickness regularization parameters chosen via an L-curve approach coincided with those resulting in the lowest achieved MAE with observed thicknesses, indicating that in the absence  
495 of thickness observations (the situation for most glaciers), picking the right regularization parameter is an effective way to ensure accuracy. However, the lowest achieved mean absolute error was above 40 m, which is relatively large for this glacier: its maximum observed thickness is 287 m. The high errors present in all three non-thickness-constrained estimates (consensus, Millan, and non-thickness-constrained IGM) indicate that there is still significant bias present in all three approaches.

Our thickness-constrained inversion results demonstrate that while observational thickness data were of some value for  
500 constraining our thickness estimate of Bhote Kosi glacier, they had only a weak influence on the final thickness field, and their interpolative power was limited. However, the thickness observations were highly valuable as validation data, whether performing velocity-only or thickness-constrained inversions. Since the HMA region still has poor data coverage, further effort is required to gather more thickness observations. Contemporaneity between input data sets is especially important for dynamical consistency in modelling glaciers that are out of steady state. Since we observed that the inversion method struggles  
505 to estimate thickness in areas with a low measured surface velocity, we propose that fieldworkers should aim to measure thickness at such locations where possible, in addition to fast-flowing areas where thickness observations can aid in selecting model parameters.

Further work is required to apply our method to other glaciers. As preliminary results on other glaciers in the region were of varying quality, the optimal choice of regularization parameter may be glacier-dependent, and it may be necessary to perform  
510 L-curve analysis for individual glaciers. Future work could also consider a more robust method for determining the Arrhenius parameter, perhaps allowing for spatial variability.

*Code and data availability.* IGM is an open-source Python package available from <https://github.com/instructed-glacier-model/igm> (last access: February 9 2026). We used IGM v2.2.3 and extended the version to output optimization cost values at higher precision. The IGM version used is archived at <https://doi.org/10.5281/zenodo.18484149>. IGM configuration files, additional code, input data, and Jupyter notebooks used in plotting figures are provided at <https://doi.org/10.5281/zenodo.18495260>.  
515

## Appendix A: Convergence of inversion

Figures A1(a) and A2(a) show the convergence of the cost function (Eq. 2) over 1000 iterations of the inversion algorithm. The velocity misfit term  $\mathcal{C}^u$  and the regularization term  $\mathcal{R}^h$  both appear to converge to a constant value after around 100–200 iterations, with only small fluctuations thereafter. In the case of the thickness-constrained inversion (Fig. A2(a)), the thickness  
520 misfit term  $\mathcal{C}^h$  behaves similarly, converging fairly soon after initialization and exhibiting only small fluctuations thereafter. On the other hand, the penalty term  $\mathcal{P}^h$  behaves as if it is either “on” (a very high number) or “off” (zero or very close,

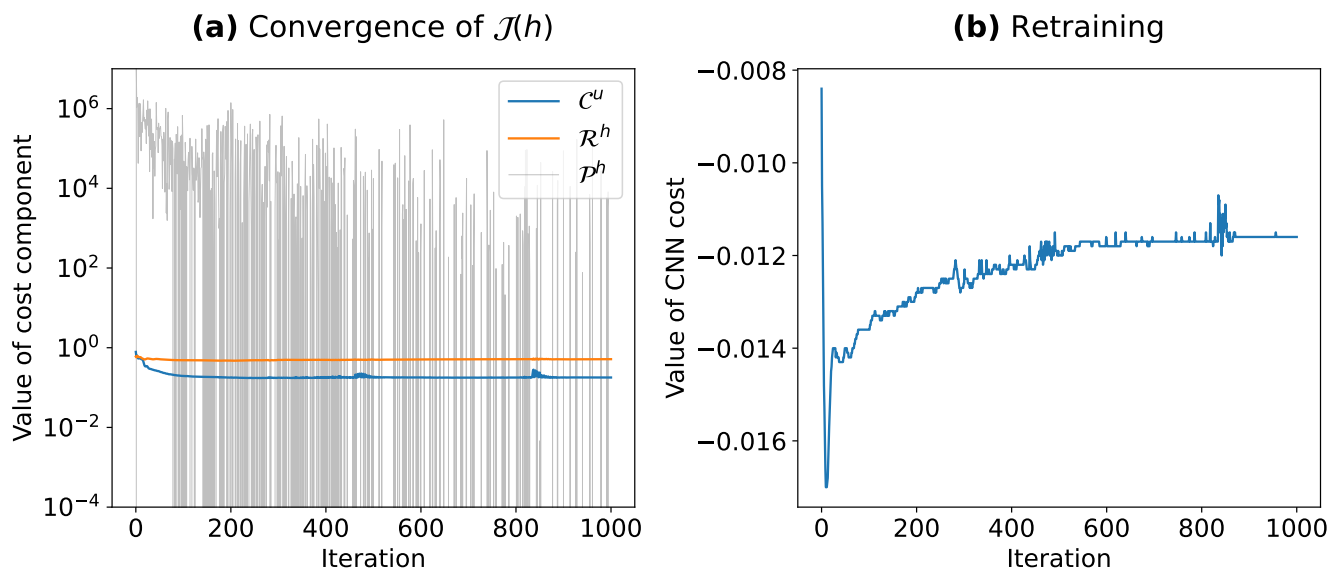


**Figure A1.** Progression of (a) the value of the cost function (Eq. 2) and (b) the value of the neural network emulator cost, over iterations of the inversion algorithm, for the velocity-only inversion with  $\alpha_h = 6$ .

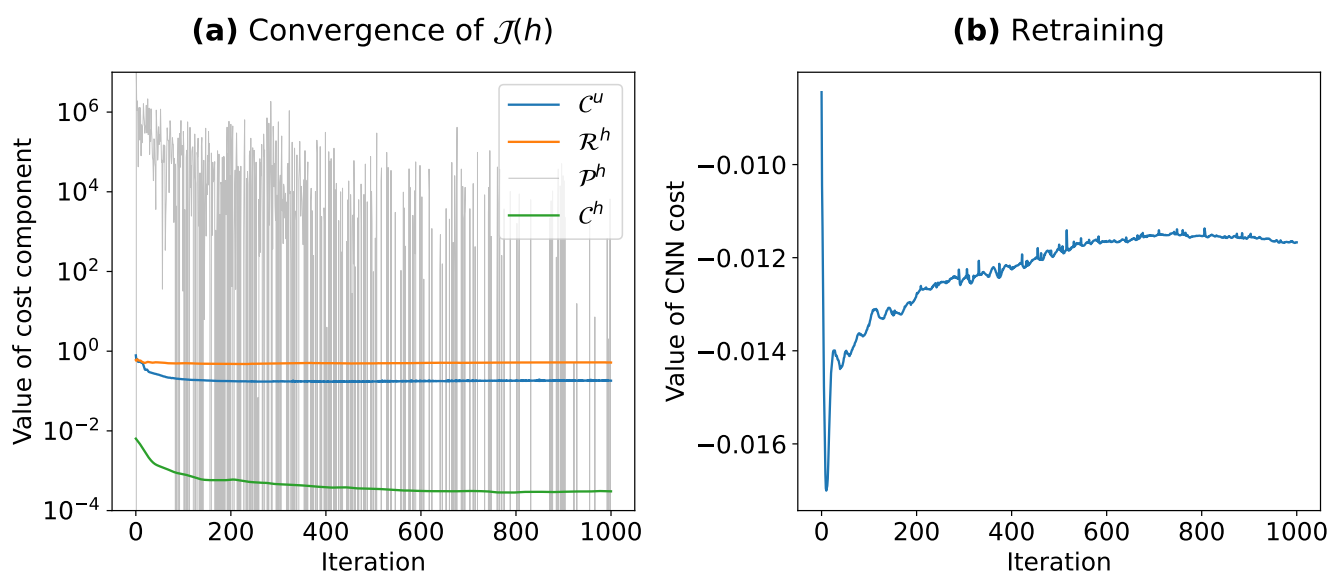


**Figure A2.** Progression of (a) the value of the cost function (Eq. 2) and (b) the value of the neural network emulator cost, over iterations of the inversion algorithm, for the thickness-constrained inversion with  $\alpha_h = 6$ ,  $\sigma_h = 300$ , and the calibration set consisting of low-elevation profiles only.



meaning there are virtually no negative thicknesses present and no positive thicknesses present outside the mask  $\mathcal{M}$ ) at each iteration. Its presence manifests as intermittent “spikes” in the cost over iterations, indicating that the inversion algorithm quickly corrects for negative thicknesses and non-zero thicknesses outside  $\mathcal{M}$ . The frequency of the spikes tends to decrease  
525 with more iterations.

Figures A1(b) and A2(b) show examples of how the neural network cost (the energy functional associated with the Blatter-Pattyn equations) evolves over the iterations of the inversion algorithm. In both cases, the cost converges towards a constant value after around 600 iterations.

### Appendix B: Presence of thickness observations outside glacier outlines

530 Figure B1 shows an example location where there are thickness observations outside the glacier outline, and where the outline does not align perfectly with the outline of the glacier in recent satellite imagery.

### Appendix C: Effect of regularization weight $\alpha_h$ on smoothness and total volume of solution

Figure C1 shows four thickness fields obtained by the velocity-only inversion, with different values of the regularization parameter  $\alpha_h$ .

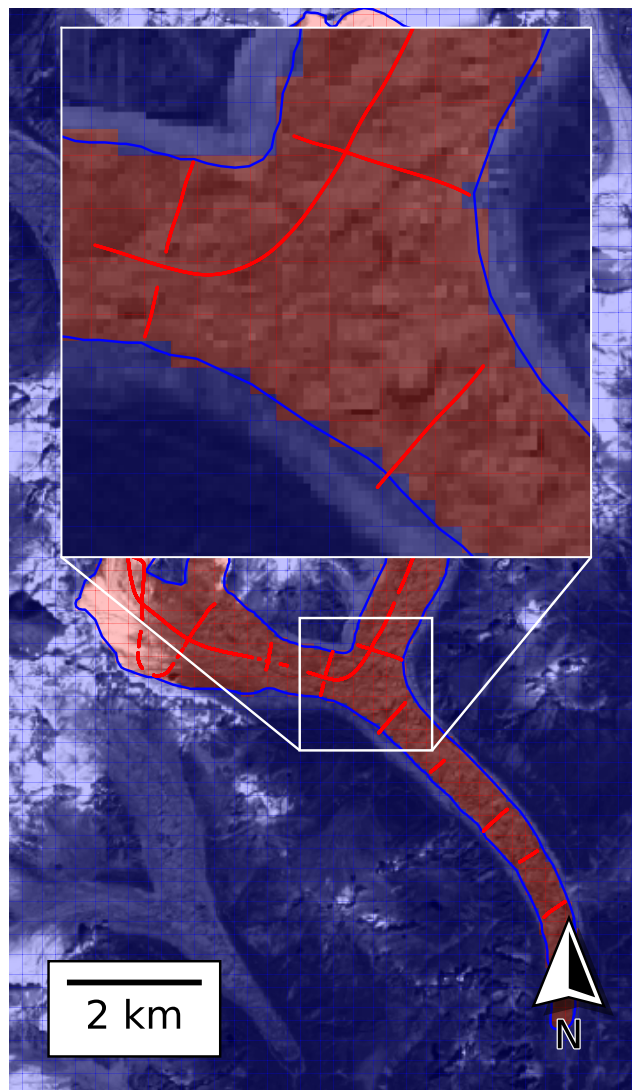
### 535 Appendix D: Exaggerated checkerboarding artefact

Figure 6(b) shows a non-physical checkerboard artefact in the tributary halfway up the north tributary of the glacier. A closer look at the input observed velocity field (Figs. 7(a), D1(a)) shows a slight discontinuity in the velocity around that location: from west to east, the speed dips from 15–20 m yr<sup>-1</sup> to around 5–10 m yr<sup>-1</sup>, and increases again to around 15–25 m yr<sup>-1</sup>, and the direction of the velocity also reverses.

540 An experiment was performed whereby the input velocity field was smoothed using a Gaussian filter with standard deviation 3 (Fig. D1(b)). We emphasize that the purpose of this experiment was solely to test the hypothesis that the jump in velocity at the problem location could be triggering non-physical artefacts in the modelled thickness field.

The resulting thickness field as estimated by IGM under a velocity-only inversion scheme is presented in Fig. D1(c). The checkerboard at that location is now less pronounced, suggesting that the jump in velocity may have triggered the artefact.

545 *Author contributions.* GS conceived the study and conducted all analysis with continuous input from DG and JM. GJ designed and provided advice on the use of IGM’s ice flow emulator and inversion methodology. HP provided ice thickness observation data. GS wrote the manuscript with review and input from all authors.



**Figure B1.** RGI v6.0 outline of Bhote Kosi glacier in blue. Locations of Pritchard et al. (2026) thickness observations in red. Red/blue overlay denotes the area inside/outside the rasterized glacier mask. Background image is a Sentinel-2 scene (band 04) from 15 October 2019 (contains modified Copernicus Sentinel data [2019] processed by Sentinel Hub).

*Competing interests.* The authors declare that they have no conflict of competing interest.

*Acknowledgements.* Gillian Smith was supported by the Natural Environment Research Council (NERC) Satellite Data in Environmental  
550 Science (SENSE) Centre for Doctoral Training [grant no. NE/T00939X/1].

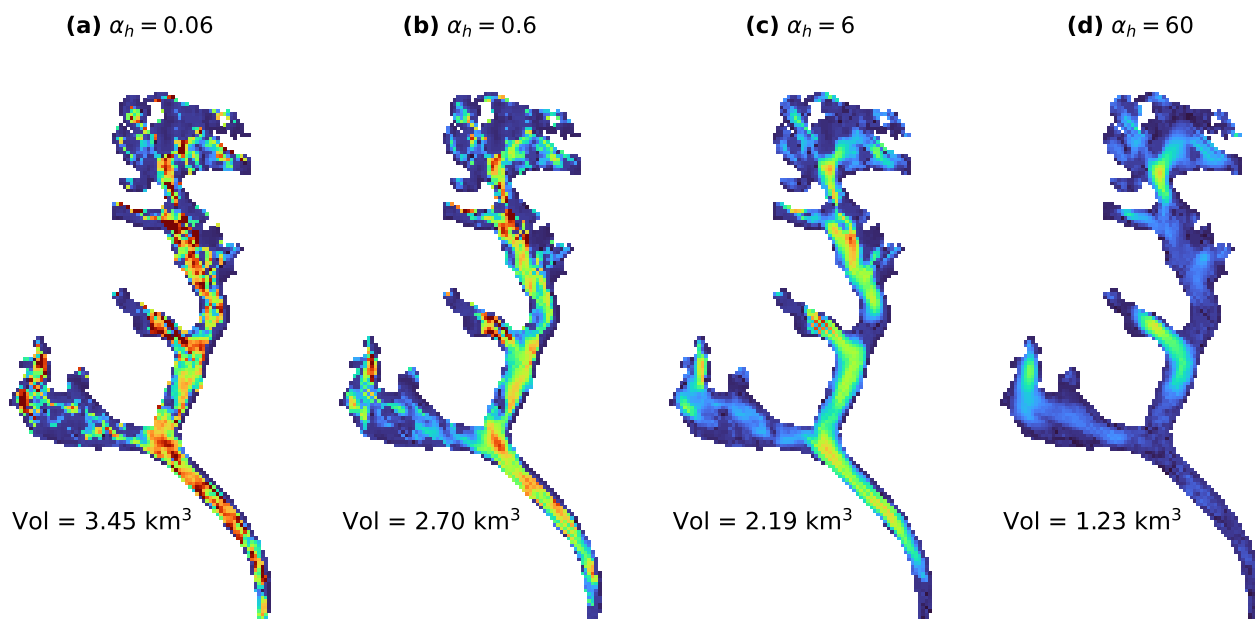


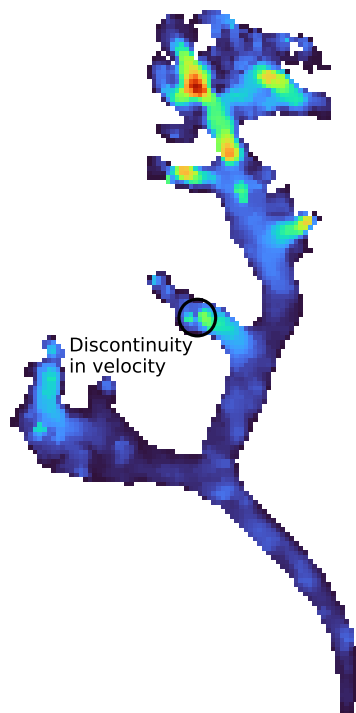
**Figure C1.** Thickness maps of Bhote Kosi glacier for four different choices of the thickness regularization parameter  $\alpha_h$ : (a)  $\alpha_h = 0.06$ , (b)  $\alpha_h = 0.6$ , (c)  $\alpha_h = 6$ , (d)  $\alpha_h = 60$ . The colour scale for all panels is identical to that of Fig. 6(a,b).

## References

- Abadi, M., Agarwal, A., Barham, P., Brevdo, E., Chen, Z., Citro, C., Corrado, G. S., Davis, A., Dean, J., Devin, M., Ghemawat, S., Goodfellow, I., Harp, A., Irving, G., Isard, M., Jia, Y., Jozefowicz, R., Kaiser, L., Kudlur, M., Levenberg, J., Mané, D., Monga, R., Moore, S., Murray, D., Olah, C., Schuster, M., Shlens, J., Steiner, B., Sutskever, I., Talwar, K., Tucker, P., Vanhoucke, V., Vasudevan, V., Viégas, F., Vinyals, O., Warden, P., Wattenberg, M., Wicke, M., Yu, Y., and Zheng, X.: TensorFlow: Large-scale machine learning on heterogeneous systems, <https://www.tensorflow.org/>, 2015.
- 555 Bosson, J. B., Huss, M., Cauvy-Fraunié, S., Clément, J. C., Costes, G., Fischer, M., Poulénard, J., and Arthaud, F.: Future emergence of new ecosystems caused by glacial retreat, *Nature*, 620, 562–569, <https://doi.org/10.1038/s41586-023-06302-2>, 2023.
- Chollet, F.: Keras, <https://keras.io>, 2015.
- 560 Cook, S. J., Jouvét, G., Millan, R., Rabatel, A., Zekollari, H., and Dussailant, I.: Committed Ice Loss in the European Alps Until 2050 Using a Deep-Learning-Aided 3D Ice-Flow Model With Data Assimilation, *Geophysical Research Letters*, 50, <https://doi.org/10.1029/2023GL105029>, 2023.
- Copernicus: Copernicus DEM GLO-90, <https://doi.org/https://doi.org/10.5270/ESA-c5d3d65>, 2019.
- Cuffey, K. M. and Paterson, W. S. B.: *The Physics of Glaciers*, Butterworth-Heinemann/Elsevier, Burlington, MA, fourth edn., ISBN 978-0-565 12-369461-4, 2010.



**(a)** Non-smoothed velocity



**(b)** Smoothed velocity



**(c)** IGM thickness (velocity-only)  
with  $\alpha_h = 6$

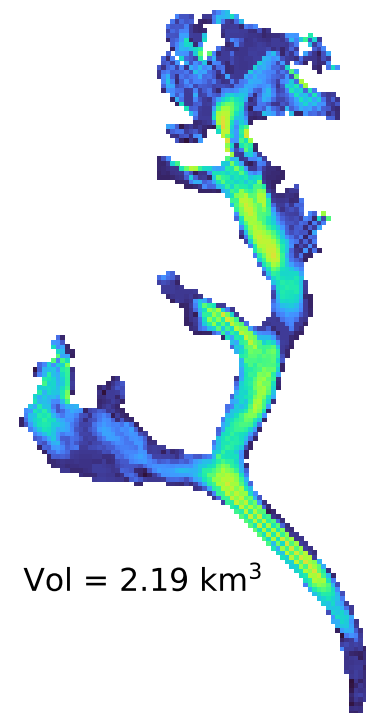


**Figure D1.** (a) Identical data and colour scale to Fig. 7(a) but only velocity magnitude is shown, (b) smoothed version of the input velocity field shown in Fig. 7(a) with only velocity magnitude shown, and (c) the resulting thickness field as estimated by IGM under a velocity-only inversion scheme with regularization parameter  $\alpha_h = 6$  and attempting to match the velocity data shown in (b), with the same colour scale as Fig. 6(a,b).



- Dehecq, A., Gourmelen, N., Gardner, A. S., Brun, F., Goldberg, D., Nienow, P. W., Berthier, E., Vincent, C., Wagnon, P., and Trouvé, E.: Twenty-first century glacier slowdown driven by mass loss in High Mountain Asia, *Nature Geoscience*, 12, 22–27, <https://doi.org/10.1038/s41561-018-0271-9>, 2019.
- 570 Farinotti, D., Brinkerhoff, D. J., Clarke, G. K. C., Fürst, J. J., Frey, H., Gantayat, P., Gillet-Chaulet, F., Girard, C., Huss, M., Leclercq, P. W., Linsbauer, A., Machguth, H., Martin, C., Maussion, F., Morlighem, M., Mosbeux, C., Pandit, A., Portmann, A., Rabatel, A., Ramsankaran, R., Reerink, T. J., Sanchez, O., Stenoft, P. A., Singh Kumari, S., van Pelt, W. J. J., Anderson, B., Benham, T., Binder, D., Dowdeswell, J. A., Fischer, A., Helfricht, K., Kutuzov, S., Lavrentiev, I., McNabb, R., Gudmundsson, G. H., Li, H., and Andreassen, L. M.: How accurate are estimates of glacier ice thickness? Results from ITMIX, the Ice Thickness Models Intercomparison eXperiment, *The Cryosphere*, 11, 949–970, <https://doi.org/10.5194/tc-11-949-2017>, 2017.
- 575 Farinotti, D., Huss, M., Fürst, J. J., Landmann, J., Machguth, H., Maussion, F., and Pandit, A.: A consensus estimate for the ice thickness distribution of all glaciers on Earth, *Nature Geoscience*, 12, 168–173, <https://doi.org/10.1038/s41561-019-0300-3>, 2019.
- Farinotti, D., Brinkerhoff, D. J., Fürst, J. J., Gantayat, P., Gillet-Chaulet, F., Huss, M., Leclercq, P. W., Maurer, H., Morlighem, M., Pandit, A., Rabatel, A., Ramsankaran, R., Reerink, T. J., Robo, E., Rouges, E., Tamre, E., van Pelt, W. J. J., Werder, M. A., Azam, M. F., Li, H., and Andreassen, L. M.: Results from the Ice Thickness Models Intercomparison eXperiment Phase 2 (ITMIX2), *Frontiers in Earth*
- 580 *Science*, 8, <https://doi.org/10.3389/feart.2020.571923>, 2021.
- Frank, T. and van Pelt, W. J. J.: Ice volume and thickness of all Scandinavian glaciers and ice caps, *Journal of Glaciology*, pp. 1–14, <https://doi.org/10.1017/jog.2024.25>, 2024.
- Gardner, A. S., Greene, C. A., Kennedy, J. H., Fahnestock, M. A., Liukis, M., López, L. A., Lei, Y., Scambos, T. A., and Dehecq, A.: ITS\_LIVE global glacier velocity data in near-real time, *The Cryosphere*, 19, 3517–3533, <https://doi.org/10.5194/tc-19-3517-2025>, 2025.
- 585 Glen, J. W.: Rate of Flow of Polycrystalline Ice, *Nature*, 172, 721–722, <https://doi.org/10.1038/172721a0>, 1953.
- Goldberg, D. N. and Heimbach, P.: Parameter and state estimation with a time-dependent adjoint marine ice sheet model, *The Cryosphere*, 7, 1659–1678, <https://doi.org/10.5194/tc-7-1659-2013>, 2013.
- Hansen, P. C. and O’Leary, D. P.: The Use of the L-Curve in the Regularization of Discrete Ill-Posed Problems, *SIAM Journal on Scientific Computing*, 14, 1487–1503, <https://doi.org/10.1137/0914086>, 1993.
- 590 Hugonnet, R., McNabb, R., Berthier, E., Menounos, B., Nuth, C., Girod, L., Farinotti, D., Huss, M., Dussaillant, I., Brun, F., and Käab, A.: Accelerated global glacier mass loss in the early twenty-first century, *Nature*, 592, 726–731, <https://doi.org/10.1038/s41586-021-03436-z>, 2021.
- Huss, M. and Farinotti, D.: Distributed ice thickness and volume of all glaciers around the globe, *Journal of Geophysical Research: Earth Surface*, 117, <https://doi.org/10.1029/2012JF002523>, 2012.
- 595 Immerzeel, W. W., Lutz, A. F., Andrade, M., Bahl, A., Biemans, H., Bolch, T., Hyde, S., Brumby, S., Davies, B. J., Elmore, A. C., Emmer, A., Feng, M., Fernández, A., Haritashya, U., Kargel, J. S., Koppes, M., Kraaijenbrink, P. D. A., Kulkarni, A. V., Mayewski, P. A., Nepal, S., Pacheco, P., Painter, T. H., Pellicciotti, F., Rajaram, H., Rupper, S., Sinisalo, A., Shrestha, A. B., Viviroli, D., Wada, Y., Xiao, C., Yao, T., and Baillie, J. E. M.: Importance and vulnerability of the world’s water towers, *Nature*, 577, 364–369, <https://doi.org/10.1038/s41586-019-1822-y>, 2020.
- 600 Jakob, L. and Gourmelen, N.: Glacier Mass Loss Between 2010 and 2020 Dominated by Atmospheric Forcing, *Geophysical Research Letters*, 50, e2023GL102954, <https://doi.org/10.1029/2023GL102954>, 2023.
- Jouvet, G.: Inversion of a Stokes glacier flow model emulated by deep learning, *Journal of Glaciology*, 69, 13–26, <https://doi.org/10.1017/jog.2022.41>, 2023.



- Jouvet, G. and Cordonnier, G.: Ice-flow model emulator based on physics-informed deep learning, *Journal of Glaciology*, 69, 1941–1955, <https://doi.org/10.1017/jog.2023.73>, 2023.
- Jouvet, G., Cordonnier, G., Kim, B., Lüthi, M., Vieli, A., and Aschwanden, A.: Deep learning speeds up ice flow modelling by several orders of magnitude, *Journal of Glaciology*, 68, 651–664, <https://doi.org/10.1017/jog.2021.120>, 2022.
- Khanal, S., Lutz, A., Kraaijenbrink, P. D. A., van den Hurk, B., Yao, T., and Immerzeel, W. W.: Variable 21st Century Climate Change Response for Rivers in High Mountain Asia at Seasonal to Decadal Time Scales, *Water Resources Research*, 57, e2020WR029266, <https://doi.org/10.1029/2020WR029266>, 2021.
- Kharazmi, E., Zhang, Z., and Karniadakis, G. E.: Variational Physics-Informed Neural Networks For Solving Partial Differential Equations, <http://arxiv.org/abs/1912.00873>, arXiv [preprint], 2019.
- Kingma, D. P. and Ba, J.: Adam: A Method for Stochastic Optimization, <https://doi.org/10.48550/arXiv.1412.6980>, arXiv [preprint], 2017.
- Kneib, M., Dehecq, A., Gilbert, A., Basset, A., Miles, E. S., Jouvet, G., Jourdain, B., Ducasse, E., Beraud, L., Rabatel, A., Mouginot, J., Carcanade, G., Laarman, O., Brun, F., and Six, D.: Distributed surface mass balance of an avalanche-fed glacier, *The Cryosphere*, 18, 5965–5983, <https://doi.org/10.5194/tc-18-5965-2024>, 2024.
- MacAyeal, D. R.: The basal stress distribution of Ice Stream E, Antarctica, inferred by control methods, *Journal of Geophysical Research: Solid Earth*, 97, 595–603, <https://doi.org/10.1029/91JB02454>, 1992.
- Maffezzoli, N., Rignot, E., Barbante, C., Petersen, T., and Vascon, S.: A gradient-boosted tree framework to model the ice thickness of the world’s glaciers (IceBoost v1.1), *Geoscientific Model Development*, 18, 2545–2568, <https://doi.org/10.5194/gmd-18-2545-2025>, publisher: Copernicus GmbH, 2025.
- Maussion, F., Butenko, A., Champollion, N., Dusch, M., Eis, J., Fourteau, K., Gregor, P., Jarosch, A. H., Landmann, J., Oesterle, F., Recinos, B., Rothenpieler, T., Vlug, A., Wild, C. T., and Marzeion, B.: The Open Global Glacier Model (OGGM) v1.1, *Geoscientific Model Development*, 12, 909–931, <https://doi.org/10.5194/gmd-12-909-2019>, 2019.
- Miles, K. E., Hubbard, B., Quincey, D. J., Miles, E. S., Sherpa, T. C., Rowan, A. V., and Doyle, S. H.: Polythermal structure of a Himalayan debris-covered glacier revealed by borehole thermometry, *Scientific Reports*, 8, 16 825, <https://doi.org/10.1038/s41598-018-34327-5>, 2018.
- Millan, R., Mouginot, J., Rabatel, A., and Morlighem, M.: Ice velocity and thickness of the world’s glaciers, *Nature Geoscience*, 15, 124–129, <https://doi.org/10.1038/s41561-021-00885-z>, 2022.
- Morlighem, M., Williams, C. N., Rignot, E., An, L., Arndt, J. E., Bamber, J. L., Catania, G., Chauché, N., Dowdeswell, J. A., Dorschel, B., Fenty, I., Hogan, K., Howat, I., Hubbard, A., Jakobsson, M., Jordan, T. M., Kjeldsen, K. K., Millan, R., Mayer, L., Mouginot, J., Noël, B. P. Y., O’Cofaigh, C., Palmer, S., Rysgaard, S., Seroussi, H., Siegert, M. J., Slabon, P., Straneo, F., van den Broeke, M. R., Weinrebe, W., Wood, M., and Zinglensen, K. B.: BedMachine v3: Complete Bed Topography and Ocean Bathymetry Mapping of Greenland From Multibeam Echo Sounding Combined With Mass Conservation, *Geophysical Research Letters*, 44, 11,051–11,061, <https://doi.org/10.1002/2017GL074954>, 2017.
- Nie, Y., Pritchard, H. D., Liu, Q., Hennig, T., Wang, W., Wang, X., Liu, S., Nepal, S., Samyn, D., Hewitt, K., and Chen, X.: Glacial change and hydrological implications in the Himalaya and Karakoram, *Nature Reviews Earth & Environment*, 2, 91–106, <https://doi.org/10.1038/s43017-020-00124-w>, 2021.
- Nixon-Hill, R. W., Shapero, D., Cotter, C. J., and Ham, D. A.: Consistent point data assimilation in Firedrake and Icepack, *Geoscientific Model Development*, 17, 5369–5386, <https://doi.org/10.5194/gmd-17-5369-2024>, 2024.



- Nocedal, J. and Wright, S. J.: Numerical Optimization, Springer Series in Operations Research and Financial Engineering, Springer New York, ISBN 978-0-387-30303-1, <https://doi.org/10.1007/978-0-387-40065-5>, 2006.
- Pattyn, F.: A new three-dimensional higher-order thermomechanical ice sheet model: Basic sensitivity, ice stream development, and ice flow across subglacial lakes, *Journal of Geophysical Research: Solid Earth*, 108, <https://doi.org/10.1029/2002JB002329>, 2003.
- 645 Picard, R. R. and Cook, R. D.: Cross-Validation of Regression Models, *Journal of the American Statistical Association*, 79, 575–583, <https://doi.org/10.2307/2288403>, 1984.
- Pritchard, H. D.: Asia’s shrinking glaciers protect large populations from drought stress, *Nature*, 569, 649–654, <https://doi.org/10.1038/s41586-019-1240-1>, 2019.
- Pritchard, H. D., Fretwell, P. T., Fremand, A. C., Bodart, J. A., Kirkham, J. D., Aitken, A., Bamber, J., Bell, R., Bianchi, C., Bingham, R. G., Blankenship, D. D., Casassa, G., Christianson, K., Conway, H., Corr, H. F. J., Cui, X., Damaske, D., Damm, V., Dorschel, B., Drews, R., Eagles, G., Eisen, O., Eisermann, H., Ferraccioli, F., Field, E., Forsberg, R., Franke, S., Goel, V., Gogineni, S. P., Greenbaum, J., Hills, B., Hindmarsh, R. C. A., Hoffman, A. O., Holschuh, N., Holt, J. W., Humbert, A., Jacobel, R. W., Jansen, D., Jenkins, A., Jokat, W., Jong, L., Jordan, T. A., King, E. C., Kohler, J., Krabill, W., Maton, J., Gillespie, M. K., Langley, K., Lee, J., Leitchenkov, G., Leuschen, C., Luyendyk, B., MacGregor, J. A., MacKie, E., Moholdt, G., Matsuoka, K., Morlighem, M., Mouginot, J., Nitsche, F. O., Nost, O. A., Paden, J., Pattyn, F., Popov, S., Rignot, E., Rippin, D. M., Rivera, A., Roberts, J. L., Ross, N., Ruppel, A., Schroeder, D. M., Siegert, M. J., Smith, A. M., Steinhage, D., Studinger, M., Sun, B., Tabacco, I., Tinto, K. J., Urbini, S., Vaughan, D. G., Wilson, D. S., Young, D. A., and Zirizzotti, A.: Bedmap3 updated ice bed, surface and thickness gridded datasets for Antarctica, *Scientific Data*, 12, 414, <https://doi.org/10.1038/s41597-025-04672-y>, 2025.
- 655 Pritchard, H. D., King, E. C., Goodger, D. J., Boyle, D., Goldberg, D. N., Recinos, B., Orr, A., and Regmi, D.: Towards Bedmap Himalayas: a new airborne glacier thickness survey in Khumbu Himal, Nepal, *Earth System Science Data*, 18, 199–217, <https://doi.org/10.5194/essd-18-199-2026>, 2026.
- RGI Consortium: Randolph Glacier Inventory - A Dataset of Global Glacier Outlines (NSIDC-0070, Version 6), <https://doi.org/10.7265/4m1f-gd79>, 2017.
- Robinson, A., Goldberg, D., and Lipscomb, W. H.: A comparison of the stability and performance of depth-integrated ice-dynamics solvers, *The Cryosphere*, 16, 689–709, <https://doi.org/10.5194/tc-16-689-2022>, 2022.
- 665 Rounce, D. R., Hock, R., and Shean, D. E.: Glacier Mass Change in High Mountain Asia Through 2100 Using the Open-Source Python Glacier Evolution Model (PyGEM), *Frontiers in Earth Science*, 7, <https://doi.org/10.3389/feart.2019.00331>, 2020.
- Rounce, D. R., Hock, R., Maussion, F., Hugonnet, R., Kochtitzky, W., Huss, M., Berthier, E., Brinkerhoff, D., Compagno, L., Copland, L., Farinotti, D., Menounos, B., and McNabb, R. W.: Global glacier change in the 21st century: Every increase in temperature matters, *Science (New York, N.Y.)*, 379, 78–83, <https://doi.org/10.1126/science.abo1324>, 2023.
- 670 Schmitt, P., Maussion, F., Goldberg, D. N., and Gregor, P.: The Open Global Glacier Data Assimilation Framework (AGILE) v0.1, EGU sphere [preprint], <https://doi.org/10.5194/egusphere-2025-3401>, 2025.
- Schoof, C. and Hewitt, I.: Ice-Sheet Dynamics, *Annual Review of Fluid Mechanics*, 45, 217–239, <https://doi.org/10.1146/annurev-fluid-011212-140632>, 2013.
- 675 Sommer, C., Malz, P., Seehaus, T. C., Lippl, S., Zemp, M., and Braun, M. H.: Rapid glacier retreat and downwasting throughout the European Alps in the early 21st century, *Nature Communications*, 11, 3209, <https://doi.org/10.1038/s41467-020-16818-0>, 2020.
- Steidl, V., Bamber, J. L., and Zhu, X. X.: Physics-aware machine learning for glacier ice thickness estimation: a case study for Svalbard, *The Cryosphere*, 19, 645–661, <https://doi.org/10.5194/tc-19-645-2025>, 2025.



- van Pelt, W. and Frank, T.: New glacier thickness and bed topography maps for Svalbard, *The Cryosphere*, 19, 1–17,  
680 <https://doi.org/10.5194/tc-19-1-2025>, 2025.
- Welty, E., Zemp, M., Navarro, F., Huss, M., Fürst, J. J., Gärtner-Roer, I., Landmann, J., Machguth, H., Naegeli, K., Andreassen, L. M.,  
Farinotti, D., Li, H., and Contributors, G.: Worldwide version-controlled database of glacier thickness observations, *Earth System Science*  
*Data*, 12, 3039–3055, <https://doi.org/10.5194/essd-12-3039-2020>, 2020.
- Wouters, B., Gardner, A. S., and Moholdt, G.: Global Glacier Mass Loss During the GRACE Satellite Mission (2002-2016), *Frontiers in*  
685 *Earth Science*, 7, <https://doi.org/10.3389/feart.2019.00096>, 2019.
- Zekollari, H., Huss, M., Schuster, L., Maussion, F., Rounce, D. R., Aguayo, R., Champollion, N., Compagno, L., Hugonnet, R., Marzeion,  
B., Mojtabavi, S., and Farinotti, D.: Twenty-first century global glacier evolution under CMIP6 scenarios and the role of glacier-specific  
observations, *The Cryosphere*, 18, 5045–5066, <https://doi.org/10.5194/tc-18-5045-2024>, 2024.
- Zheng, G., Allen, S. K., Bao, A., Ballesteros-Cánovas, J. A., Huss, M., Zhang, G., Li, J., Yuan, Y., Jiang, L., Yu, T., Chen, W., and  
690 Stoffel, M.: Increasing risk of glacial lake outburst floods from future Third Pole deglaciation, *Nature Climate Change*, 11, 411–417,  
<https://doi.org/10.1038/s41558-021-01028-3>, 2021.